Experimental investigation of Z-pinch radiation source for indirect drive inertial confinement fusion

View Online   Export Citation   CrossMark

Zhenghong Li, Zhen Wang,[a] Rongkun Xu, Jianlun Yang, Fan Ye, Yanyun Chu, Zeping Xu, Faxin Chen, Shijian Meng, Jianmin Qi, Qinyuan Hu, Yi Qin, Jiaming Ning, Zhanchang Huang, Linbo Li, and Shuqing Jiang

AFFILIATIONS

Institute of Nuclear Physics and Chemistry, China Academy of Engineering Physics, Mianyang 621900, China

[a] Author to whom correspondence should be addressed: wangz_es@caep.cn

ABSTRACT

Z-pinch dynamic hohlraums (ZPDHs) could potentially be used to drive inertial confinement fusion targets. Double- or multishell capsules using the technique of volume ignition could exploit the advantages of ZPDHs while tolerating their radiation asymmetry, which would be unacceptable for a central ignition target. In this paper, we review research on Z-pinch implosions and ZPDHs for indirect drive targets at the Institute of Nuclear Physics and Chemistry, China Academy of Engineering Physics. The characteristics of double-shell targets and the associated technical requirements are analyzed through a one-dimensional computer code developed from MULTI-IFE. Some key issues regarding the establishment of suitable sources for dynamic hohlraums are introduced, such as soft X-ray power optimization, novel methods for plasma profile modulation, and the use of thin-shell liner implosions to inhibit the generation of prior-stagnated plasma. Finally, shock propagation and radiation characteristics in a ZPDH are presented and discussed, together with some plans for future work.

I. INTRODUCTION

Owing to their high conversion efficiency of up to 15% from stored electrical energy to X-rays,[1] fast Z pinches, as intense laboratory soft X-ray (SXR) sources, show great promise for driving inertial confinement fusion (ICF).[2] Different approaches have been developed with the goal of ignition using Z-pinch implosions. A well-known example is central hot-spot ignition, which is similar in concept to the laser-driven cylindrical hohlraum ICF approach at the National Ignition Facility. In central hot-spot ignition, a low-density "hot spot" at the center of compressed high-density and "cold" fuel in a capsule centered in a Z-pinch-driven hohlraum (ZPDH)[3–6] or a cylindrical double-Z-pinch-driven secondary hohlraum[7,8] is ignited with minimum driver energy and high convergence requirement. A thermonuclear neutron yield of 3.5×10^{11} was obtained in experiments on the 20-MA Z machine.[9] Following refurbishment of the Z machine (to give the ZR machine), a magnetic direct drive approach named MagLIF has been proposed, in which a heavy beryllium liner is imploded to directly compress the DT fuel, and the fuel is magnetized by an external current coil and preheated by a laser pulse to lower the convergence requirement.[10,11] Integrated MagLIF experiments have

produced more than 10^{12} thermonuclear DD neutrons in one shot on the ZR machine. In 2016, a magnetic indirect drive approach was introduced.[12] This uses a ZPDH to drive a double-shell capsule. DT fuels are typically surrounded by an Au–Cu mixture. Volume ignition rather than hot-spot ignition is used with this type of capsule, so less care needs to be taken in pulse shaping, and symmetry requirements are relaxed. The ignition temperature can also be lowered to ~4 keV, which is much lower than the theoretical threshold of ~4.8 keV for central ignition. In the context of these approaches, much research, both theoretical and experimental, has been carried out on the physics of Z-pinch implosions and hohlraums since the 1990s.

Over the last two decades, fast Z pinches have been investigated at several low-current facilities: for example, gas-puff and multiwire implosions at the Yang facility of the China Academy of Engineering Physics (CAEP),[13] wire ablation processes at the PPG-1 facility at Tsinghua University (THU)[14–16] and at some smaller facilities at the Northwest Institute of Nuclear Technology (NINT) and Xi'an Jiaotong University (XJTU),[17–19] and wire-array implosions at the Qiangguang-1 facility at the NINT.[20] Joint experiments on wire-array implosions and DH hohlraums have also been performed using the

S300 and Angara-5 facilities[21,22] at the Troitsk Institute for Innovation and Thermonuclear Investigation (TRINITI). Since 2014, the ~8-MA Julong-1 facility of the CAEP has provided us with the capability to investigate ZPDHs created by wire-array implosions.[23,24]

In 2006, Peng[25] proposed a novel target design to be irradiated inside the center of a ZPDH. DT ice fuels were used to relax convergence requirements. High-Z materials surrounding the DT fuel were able to improve the performance of volume burn and relax the ignition temperature requirements to ~3 keV. This arrangement could tolerate a driving asymmetry, i.e., fluctuation of energy flux, of ~20%. Zhao *et al.*[26] explored the parameter space for a Z-pinch-driven volume ignition target. Following the proposal in 2010 for a fusion–fission hybrid concept named Z-FFR,[27] the target was further developed to provide stable and significant gain while taking into consideration the radiation symmetry and uniformity in a ZPDH.[28]

Ding *et al.*[29] have described MHD code developments and numerical studies of the physics of wire-array Z-pinches and ZPDHs over the last two decades. In this paper, we will give a general review of experimental attempts to establish suitable sources for an indirect drive target, including early work on Z-pinch radiation optimization and more recent experiments on ZPDHs at the Institute of Nuclear Physics and Chemistry, China Academy of Engineering Physics. Some key numerical results and technical requirements for the target

are introduced in Sec. II. Advances in wire-array Z-pinches and ZPDH experiments are described in Secs. III and IV. Finally, a summary together with plans for future work are presented in Sec. V.

II. VOLUME IGNITION TARGET: PERFORMANCE AND TECHNICAL REQUIREMENTS

Numerical results on the volume ignition target centered in a cylindrical hohlraum studied in this paper were obtained using a one-dimensional (1D) computer code developed from MULTI-IFE.[30] A spherical capsule centered in a cylindrical ZPDH is considered here because of its relatively high gain. The coupling problem can be avoided by having a relatively large distance between the hohlraum wall and the capsule surface when a volume ignition target is used and the hohlraum temperature is much higher than 200 eV. The simulation using a 1D code for the target is decomposed into two steps. In the first step, the dynamical behavior of the Z-pinch plasma and the hohlraum radiation is simulated with an MHD model for given current waveform, linear mass, and wire-array radius. A cylindrical simulated target is put in the hohlraum. The variations of radiation temperature $T_r(t)$ in the hohlraum are calculated. In the second step, hohlraum radiation with the same profile is used to irradiate a spherical target, and the dynamic behavior of this target is simulated using the radiative hydrodynamic code described in Ref. 31.
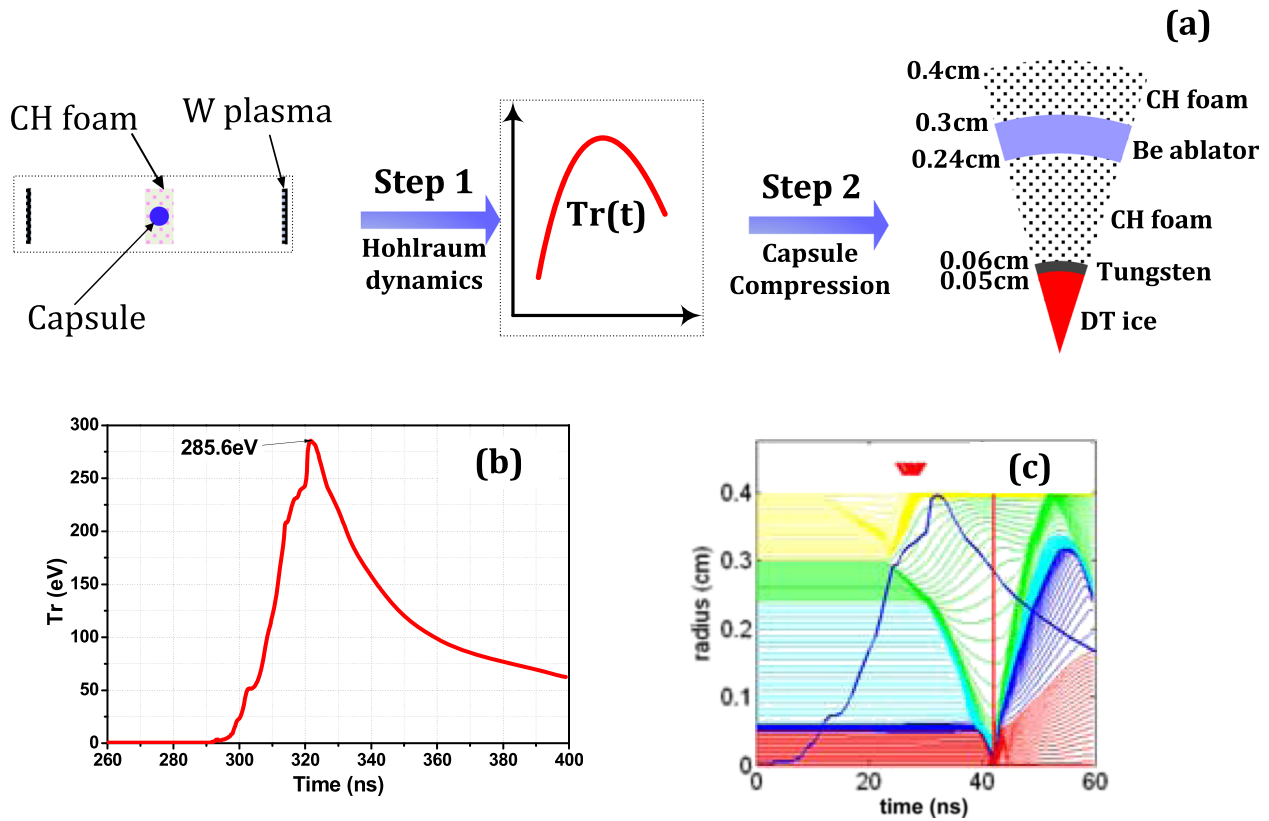

FIG. 1. (a) Scheme of the two-step simulation and configuration of the capsule. (b) Hohlraum radiation temperature profile $T_r(t)$ on the surface of the ablator simulated in step 1. (c) Implosion diagram of the target together with the driving $T_r(t)$ (blue curve) and the fusion production within ~70 ns (FWHM, red curve).

TABLE I. Target parameters.

Target	Layer (inner first)	Thickness (cm)	Density (mg/cm^3)	Mass (mg)	Material
#1: Volume ignition	1	0.05	0.25	0.13	DT
	2	0.01	18	6.86	W
	3	0.18	0.05	2.85	CH
	4	0.06	1.84	101.55	Be
	5	0.10	0.02	3.10	CH

In the present simulation, the driving current profile takes the form $I_t = I_m \sin^2 \omega t$, with a peak value of 50 MA and a 10%–90% rise time of 150 ns. The cylindrical liner has a linear mass of 20 mg/cm and an initial radius of 6.5 cm. A cylindrical double-shell simulated target with an outer ablator radius of 3 mm is centered in this 6.5-mm-radius volume filled with 10 mg/cm^3 CH foam. DT ice fuel pellets with an outer radius of 0.5 mm in the capsule are surrounded by a 0.1-mm-thick tungsten shell. The simulation results show that the load plasma attains its maximum kinetic energy of 2.62 MJ/cm at 301 ns from the start of the current. The hohlraum radiation temperature rises from ~295 ns and peaks at 321.6 ns, as shown in Fig. 1. At 319 ns, the load plasma stagnates at a radius of 4.7 mm, which is much larger than the initial radius of simulated target. Each material inside the DH hohlraum reaches its total energy peak of 4.87 MJ/cm at the same moment.

Based on this $T_r(t)$ profile, the dynamic behavior of a spherical double-shell target in this ZPDH hohlraum is simulated with target parameters (#1) as shown in Table I. Figure 2 shows the energy evolution of the implosion target. The capsule absorbs 2.8 MJ total energy from the hohlraum, 46.2 kJ of which is delivered to the DT fuel, and yields a fusion energy of 24.9 MJ with a burn ratio of 55%. The ion temperature of the DT fuels has an average value of 3.1 keV at maximum compression and peaks at more than 80 keV after ~100 ps from maximum compression.
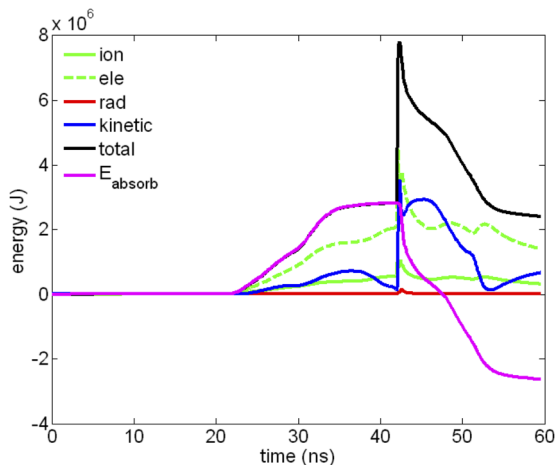
Figure 3 shows the variation of the fusion yield for the same target when the hohlraum temperature $T_r(t)$ deviates from the expected value. We use the same temperature profile, i.e., with $T_r'(t) = cT_r(t)$ as the input, where c is a constant and $T_r(t)$ is the same as in Fig. 1(b). Taking into account that the hohlraum radiation will be weaker than the numerical prediction of the 1D code, the tolerable variation of the peak T_r can be up to ~35 eV.

The volume ignition target shows good performance in suppressing the effect of fuel mixing. Reference 12, using a fall-line analysis, gives a rough loss estimate of about half the yield for a target with specified parameters. In our model, the fall-line analysis gives a loss estimate of over 99%, because of the different cross point for a different target. We consider a worst case in which a portion of the fuel is mixed with high-Z materials from the outer shell. The possible maximum mixing depth is carefully calculated according to the range of energetic high-Z particles in the compressed DT fuel. The number ratio of hydrogen isotopes vs tungsten is 3:1 in the mixing volume. The results are shown in Fig. 4 for a target with a DT radius of 0.04 cm and a Be-ablator radius of 0.2 cm. When 67.0% of the total fuel mass is mixed with shell material, the fusion energy decreases from 10.02 MJ to 6.25 MJ. At maximum compression, the radius of the DT fuel is 41.3 μm and the tolerable mixing depth is 13.8 μm.

In a low-density (10 mg/cm^3) CH foam, radiation can be transported more than 1 cm in 0.1 ns when the radiation temperature is than 200 eV. This indicates that radiation in a ZPDH could be
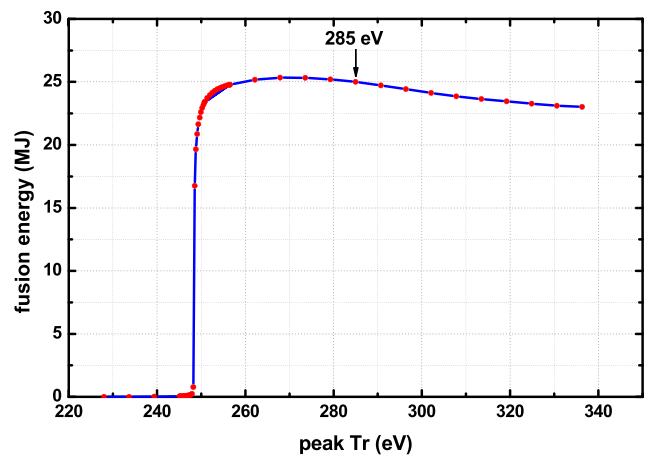

FIG. 2. Ionic and electronic internal energies, kinetic energy, and radiative energy, together with the evolution of the absorber energy of the implosion target. The internal, radiative, and kinetic energies are shown at different times, while the energy absorbed by the capsule is integrated over time.

FIG. 3. Variation of fusion yield with hohlraum temperature for the same target as in Table I.
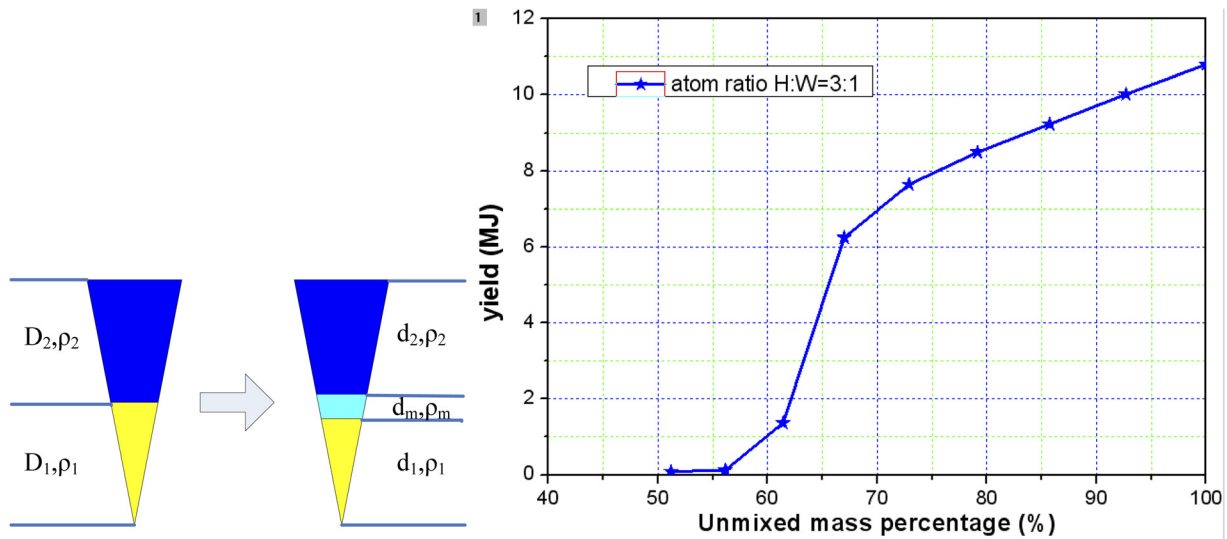
FIG. 4. (a) Model of the fuel mix of a 2-mm-radius double-shell target. The blue, yellow, and green areas represent the surrounding tungsten shell, the DT ice fuel, and mixed materials, respectively. (b) Variation of fusion yield with unmixed mass percentage.

smoothed rapidly throughout the ZPDH volume, since, in most cases, the radius of the ZPDH is less than 1 cm. Therefore, if the process of energy conversion from the kinetic energy of the Z-pinch plasma to radiation energy in the hohlraum could be finished as soon as possible, this would be of great benefit to the integral radiation symmetry in the hohlraum. Consequently, it is necessary that the plasma shell be compact and thin when it impacts on the surface of the hohlraum. On the other hand, the density of the imploding plasma affects the hohlraum radiation and the subsequent energy coupling efficiency. Since a very small sector of a spherical model of sufficiently large radius can be approximated as cylindrical, we can perform numerical simulations on the r–z plane using the 1D computer code for a cylindrical ZPDH containing a spherical capsule. In this model, the tungsten plasma will impact on a two-layer CH foam sphere with an areal kinetic energy of 1.23 MJ/cm^2. The CH foam sphere has a large radius of 35.03 cm, a 0.03-cm-thick outer shell at high density serves as a converter, and the inner shell at low density is the simulated hohlraum volume, as shown in Table II. 1D simulations are performed to determine how the interior energy fluxes change as the density of the imploding plasma decreases.

The results are given below. Figure 5 indicates that the hohlraum radiation noticeably decreases in temperature amplitude and widens in pulse width, especially when the plasma density is lower than 0.1 g/cm^3. A plasma density as low as 0.01 g/cm^3 is unacceptable, since the

radiation temperature is much lower than 200 eV. In such a case, it is difficult for the radiation to be transported smoothly inside the hohlraum, so radiation asymmetry will become a serious problem, and the ablative pressure of the Be ablator used in the ICF target will be insufficient to compress the DT fuel.

The energy coupling efficiency η is defined as $\eta = (E_r + E_P)/E_k$, where E_r, E_P, and E_k are the integrated radiative flux, the PdV work by shock pressure, and the incident kinetic energy, respectively. The variations of E_r and E_P with plasma density at different times are shown in Fig. 6. At 3 mm depth inside the hohlraum, which is the usual distance between the ablator of the target and the inside wall of the hohlraum, the effect of shock pressure is negligible because of its smaller velocity compared with that of radiation transport. This condition is also necessary to ensure that the shock does not destroy the symmetry of target compression. It can be seen from Fig. 6(b) that the maximum radiative flux occurs at ~1 ns at 3-mm depth. The corresponding energy coupling efficiencies at 1 ns are 45.7%, 35.4%, and 15.4% for plasma densities of 0.5, 0.1, and 0.05 g/cm^3, respectively, and consequently the plasma density should be much higher than 0.1 g/cm^3, which poses new challenges for wire-array implosions.

To utilize the volume ignition target in an IFE system such as Z-FFR, its gain needs to be greatly improved. Peng[28] presented a modified target configuration in which the double-shell structure

TABLE II. Simulated hohlraum parameters.

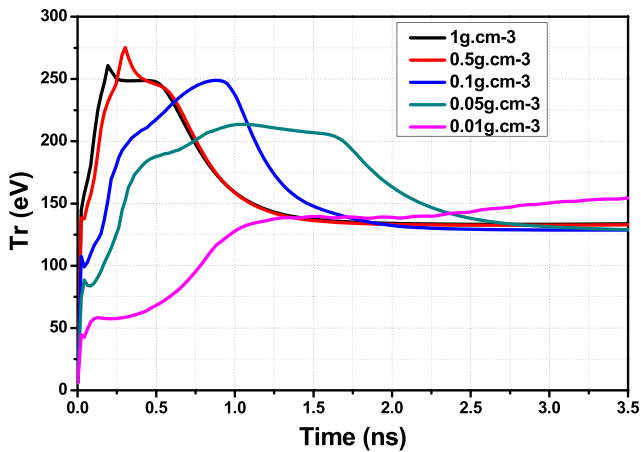| Layer (Inner first)	Thickness (cm)	Density (mg/cm^3)	Areal kinetic energy (MJ/cm^2)	Material
1	0.01	500	1.225	W
2	0.03	300	0	CH
3	35.0	15	0	CH

FIG. 5. $T_r(t)$ for interaction of imploding plasma with foam at different plasma densities on the interface between layers 2 and 3.
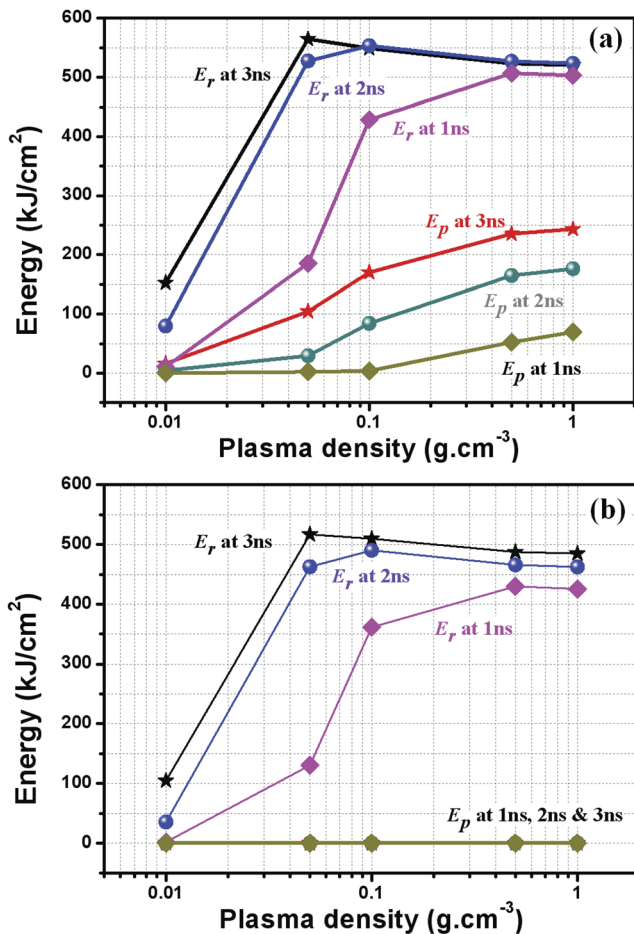

FIG. 6. Total energy, where E_r and E_P represent radiative flux and PdV work respectively, coupled inward from the imploding plasma to the hohlraum at different times: (a) on the interface between layers 2 and 3; (b) at 3-mm depth inside layer 3.

was replaced by a multishell one, with the DT fuel separated into two parts by a high-Z shell. The inner part of the fuel is compressed and ignited first. The outer part, containing most of the fuel mass, is then recompressed and heated further by alpha particles. Driven by the same $T_r(t)$ obtained at 50-MA peak current as in Fig. 1, such a multishell target could yield a fusion energy of more than 150 MJ. If the driving current were increased to 60 MA and the target parameters changed with the current, then the yield should be able to exceed 1200 MJ.[28] However, for this configuration, more attention needs to be paid to instabilities, compared with the case of a double-shell target.

III. WIRE-ARRAY IMPLOSIONS: SOFT X-RAY RADIATION AND PLASMA DYNAMICS

This section gives a brief description of the most important diagnostics used in these experiments, as well as discussing the optimization of radiation power and plasma dynamics.

A. Diagnostics

As mentioned above, experiments were performed at the 1.5-MA QiangGuang-1, 2-MA S300, 4-MA Angara-5, and 8-MA Julong-1 facilities, with more than one thousand shots. In these experiments, various types of diagnostic equipment were developed for measuring soft X-ray radiation, instantaneous imaging of moving plasma or self-emission, acquisition of X-ray spectra, and probing magnetic fields.

For X-ray radiation measurements, an SXRPM (Soft X-ray Power Meter),[32] which has a flat spectral response ranging from 100 eV to 1.2 keV and a temporal response of less than 2 ns, was used, together with a thin-foil bolometer.[33] In an SXRPM, a plastic scintillator behind a slit converts incident X-ray radiation into visible light. As a receiver, a photoelectric tube is placed at an angle of 45° to the incident direction to avoid visible light directly emitted from the
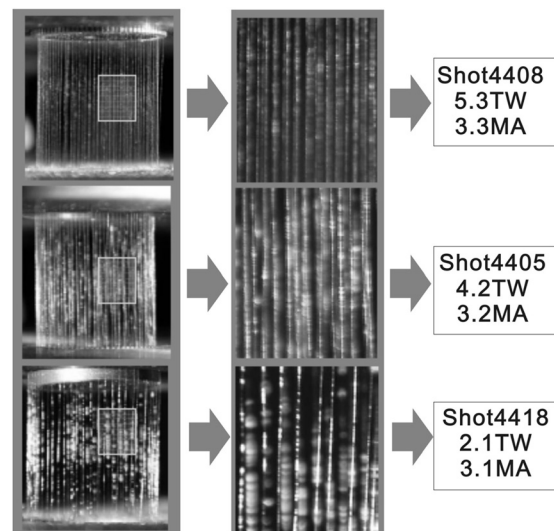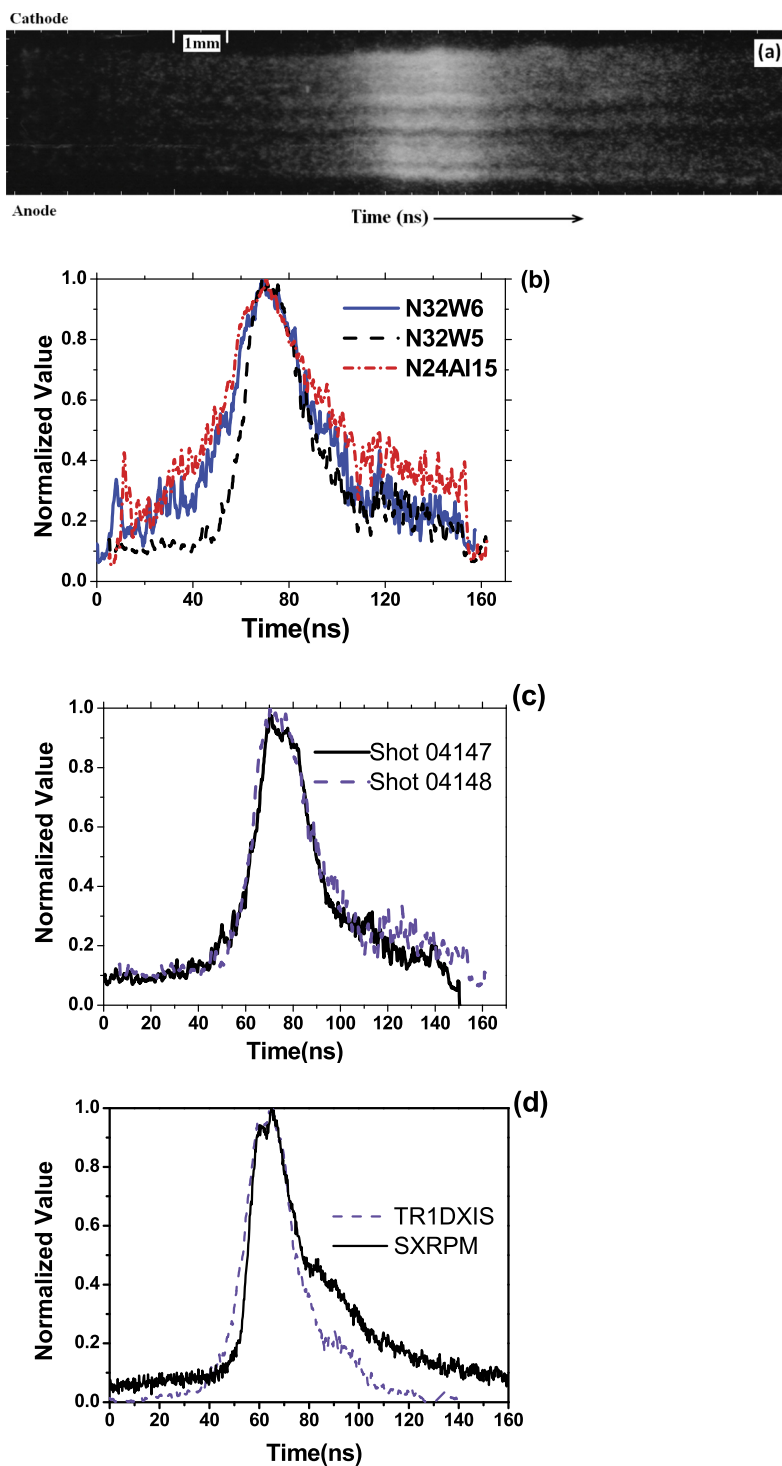

FIG. 7. Effect of the initial state of the wire array on SXR power production. The three images on the right have the same magnification factor. Reprinted with permission from Wang *et al.*, Acta Phys. Sin. **60**, 025209 (2011). Copyright 2011 the Chinese Physical Society.[22]

FIG. 8. (a) Typical axial TR1DXIS image obtained in shot 04148. On the horizontal axis, 1 mm equals 8.4 ns. The vertical axis represents the axial direction of the array. (b) Localized SXR power variation, in arbitrary spatial intervals of 1 mm along the z direction, for three kinds of load obtained at QiangGuang-1. Time benchmarks have been shifted for convenience of comparison. These loads were all 20 mm in height and 8 mm in diameter. N32W6 represents a single array comprising 32 6-μm-diameter tungsten wires. (c) Arbitrary localized SXR pulses derived from two different shots using the same N32W5 load. Reprinted with permission from Wang et al., Chin. Phys. **16**, 772 (2007). Copyright 2007 the Chinese Physical Society.[48]

pinch. A multichannel X-ray spectrometer allows determination of the distribution of X-ray radiation energy in several spectral intervals at every instant during the implosion. In some cases, a simplified SXRPM, in which the photoelectric tube is substituted by a PIN detector coupled with a 125-μm-diameter fiber, was used to measure the azimuthal distribution of X-ray emission.

An X-ray framing camera[34] based on pinhole-array imaging was used, with two configurations: a four-frame configuration with a temporal resolution of less than 100 ps and a framing interval of several hundred picoseconds between frames, and a ten-frame configuration with a temporal resolution of ~1 ns at a framing interval of 1–10 ns. Different transmission filters with photon energy up to 10 keV could be added to the pinhole array. The spatial resolution was worse than 100 μm, although a simplified pinhole camera with films and a filtered small pinhole was used when high-resolution images were required.

A 266-nm laser probe[35,36] is able to provide four to six frames in one shot with two configurations. One configuration using laser pulses as long as 10–30 ns enables free adjustment of the time interval between every two frames. It has a time resolution of 0.7–1.5 ns for different image intensifiers. The other configuration uses ~0.5-ns laser pulses for higher time resolution. The laser probe has an aperture angle of 4°–6° and a spatial resolution of ~50 μm for an imaging ratio $M = 1$. In some cases, it can also be used as a UV framing camera when the laser is removed.

When the photomultiplier tube in the SXRPM is substituted by an imaging slit and then coupled to a streak camera through a linear 125-μm-fiber array, the resulting time-resolved 1D X-ray imaging system (TR1DXIS)[37] allows direct observation of the radial or axial SXR power variation during the whole implosion. A side-on optical streak camera is usually used together with the TR1DXIS for trajectory and velocity measurements.

The X-pinch[38] is a widely used backlighting source in low-current devices for multiwire implosions, despite its disadvantages of likely multipulses and almost untunable timing. This radiographic tool was also developed[39,40] and used at the Qiangguang-1 facility.[41] Laser-irradiated point X-ray sources with photon energies of several keV, such as the Z-Beamlet on the Z machine, constitute another useful radiographic tool, especially for wire-array implosions.[42] For double-shell or multishell targets in hohlraums, X-ray radiography at tens of keV is required. A powerful new radiographic technique based on nonlinear Thomson scattering, for energies exceeding 100 keV, is now under development.[43]

Grating spectrometers were used in early experiments. Later, a bent crystal spectrometer[44] was developed in which films and imaging plates were used to measure SXR spectra integrated over implosion time. This spectrometer was also coupled with a streak camera to observe spectral variation during the whole implosion process.[45]

Furthermore, to investigate the current distribution in precursor plasmas, low-density foams in dynamic hohlraums, and nested wire arrays, a novel magnetic probe was developed.[46] An opposite-polar double-coil configuration was used to eliminate the intense electromagnetic background signal.

B. Optimization of radiation power in wire-array implosions

Wire-array implosions can produce a peak radiation power scaling approximately in proportion to the square of the maximum
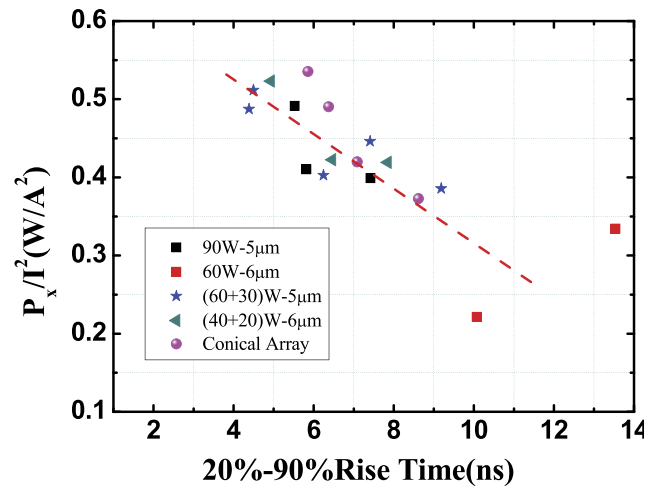
FIG. 9. Dependence of peak radiation power on the rise time of the leading edge of the power pulse. To reduce the influence of long-period precursor radiation, the starting point in the leading edge is set at 20% of the peak value. Different symbols represent different kind of loads; e.g., "90W-5μm" is a single array comprising 90 5-μm-diameter tungsten wires and "(60+30)W-5μm" is a double array with 30 wires in the inner array.

current. This type of sub-keV radiation has an approximate Planckian spectrum and can be used for ICF studies. In the Z-pinch experiments performed by CAEP on low-current facilities, X-ray radiation with peak powers from 0.5 to 5 TW and energies from 10 to 100 kJ was generated,[21,22] and the main physical processes could be replicated by numerical simulations.[47]

Implosion dynamics of single wire-array loads were investigated in low-current facilities using tungsten wires with diameter ranging from 4.2 to 6 μm.[21,22,48,49] In early experiments, plasma rings[49] were observed blasting off from both electrodes and greatly disturbing the imploding plasma. These result from the effect of field emission at
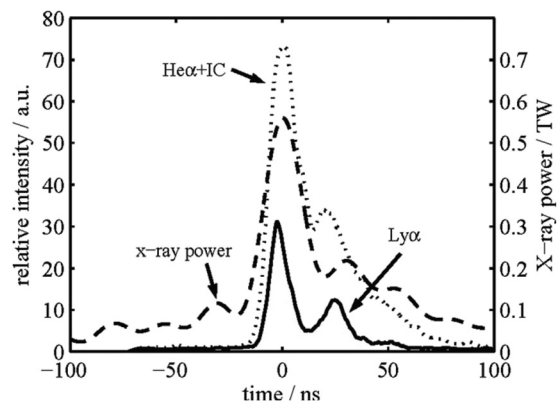
FIG. 10. Time-resolved X-ray spectrum of a double array in transparent mode imploded on the S300 facility. Time $t = 0$ corresponds to the moment when the SXR power reaches its maximum (see the dashed line). Reprinted with permission from Ye et al., Rev. Sci. Instrum. **80**, 106105 (2009). Copyright 2009 AIP Publishing LLC.[45]

fixing gaps between wires and electrodes. They can be suppressed by improving the way in which the wires are fixed to the electrodes.[50,51]

The quality of the wire-array load when it has been fixed between the electrodes of the pulsed power facility is one of the key factors affecting SXR power production. Bends in the wires and an asymmetric distribution along the circumference will seed Rayleigh–Taylor (RT) instabilities. Figure 7 shows some results obtained on the Angara-5 facility. The single-wire array comprising 90 tungsten wires 5 μm in diameter has a height of 15 mm and diameter of 12 mm.

Localized plasma dynamics also plays an important role in wire-array implosions. TR1DXIS images indicate a zipper-like effect similar to the phenomenon in gas-puff and fiber Z pinches, i.e., plasmas implode to the array axis at different moments along the z direction. This results in a widened SXR pulse and a reduced peak power. Figure 8 shows the localized SXR power pulses derived from TR1DXIS images. If we divide the image in Fig. 8(a) into small strips along the direction of the array axis (i.e., the longitudinal axis) and integrate the radiation intensity $I(z,t)$ over z, then a set of localized SXR pulses $I_z(t)$ are obtained. These pulse curves for different loads are compared in Fig. 8(b). The results from different shots show good consistency for the same kind of load. However, there are great differences for localized pulses with different kinds of load, especially at the leading edge. Temporal fluctuations of these localized pulse curves in one shot decreased

from 4.5 ns (N32W6) to 2.8 ns (N32W5). As a result, the maximum SXR power increased by a factor of ~30%.

Much work was done to improve the quality of wire-array loads using 5-μm-diameter tungsten wires. Later, 4.2-μm-diameter wires were also introduced. In a test experiment on the Qiangguang-1 facility, single arrays using these two kinds of wires produced peak radiation powers, averaged over tens of shots, of 0.49 ± 0.04 TW (4-μm W wires) and 0.48 ± 0.05 TW (5-μm W wires) when driven by a current of 1.33 ± 0.05 MA.[22]

Nested arrays can greatly improve performance. Reference 22 compares a single array and a double array with the same linear mass. Proportional to the rise time of the leading edge of an SXR pulse, temporal fluctuations for the two kinds of array are 2.0 and 1.5 ns, with overall pulse widths of 11.4 and 10.0 ns, respectively. As a result, the double array load has a peak power, averaged over several shots, 1.5 times larger than that of the single array. Figure 9 shows the relationship between peak radiation power and the fast leading edge of the power pulse for single, nested, and conical arrays. This result is consistent with both the distribution of the plasma density profile and the RT-instability-induced bubble-spike amplitude. In a double array, the subsequent current rise rate after outer/inner plasma interaction is also a key factor.

On the Angara-5 facility, the 90W-5μm single array produced an averaged power of 4.58 ± 0.56 TW, while the non-optimized
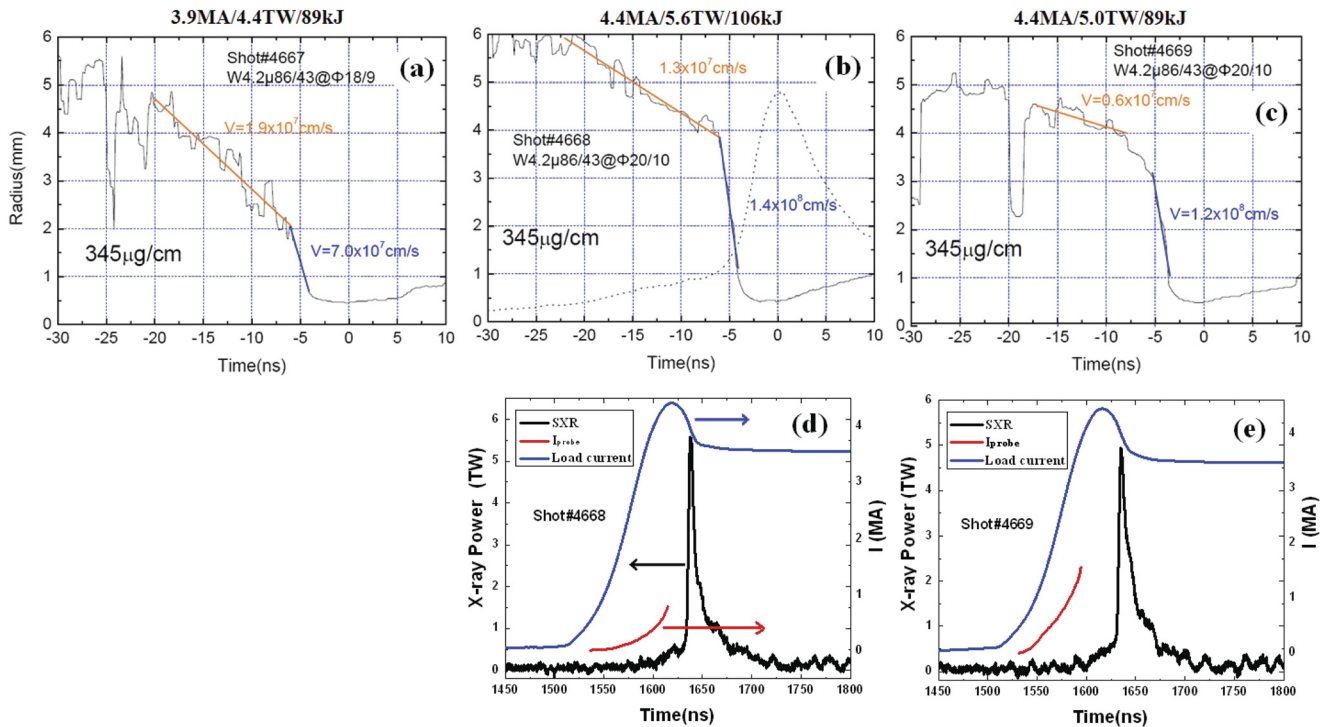
FIG. 11. Implosion trajectories derived from TR1DXIS images in three shots for two kinds of double array, together with the corresponding peak current, peak radiation power, total radiation energy, and implosion velocity. These correspond to the boundary at which the emission intensity drops to half of the peak emission. The arrays all comprised 129 4.2-μm-diameter tungsten wires. The inner array in each of these loads has radius and linear mass half those of the outer array. (a) Trajectory of shot 4667, double load with 18-mm outer radius. The horizontal axis is the time relative to the SXR maximum. (b) and (c) Trajectories of shots 4668 and 4669 for the same double load with 20-mm outer radius. The dashed line in (b) indicates the SXR pulse; (d) and (e) Current distributions and SXR pulses obtained in shots 4668 and 4669; the red lines indicates current flowing through the inner array measured by a micro magnetic probe.
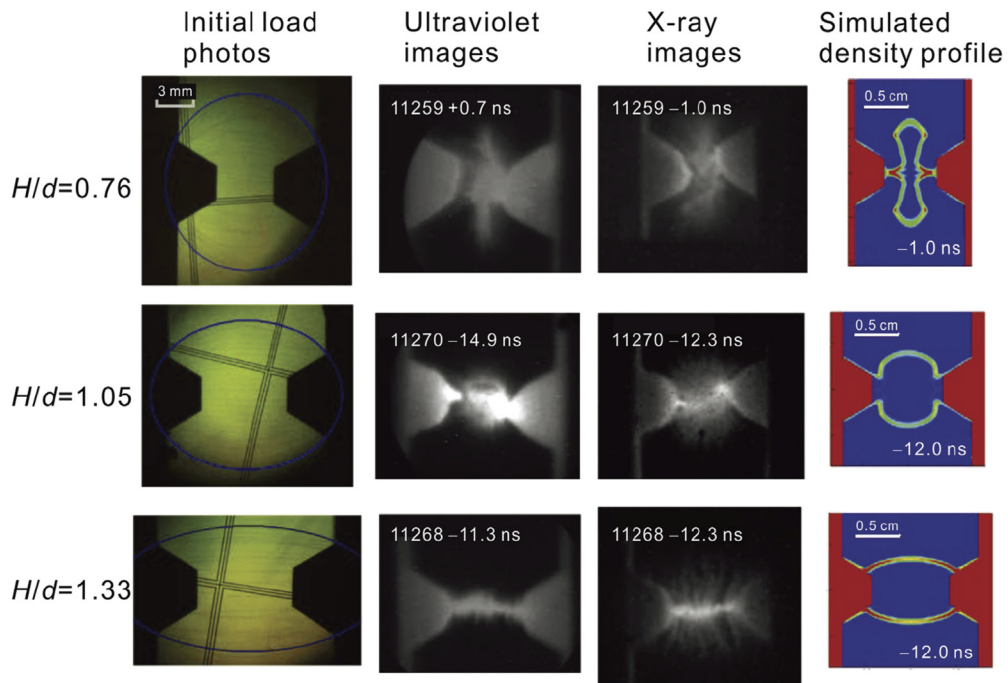
FIG. 12. Optical images taken by telescope immediately before current loading, together with UV images, X-ray images, and density profiles from 2D numerical simulations for loads with H/D ratios of 0.76, 1.05, and 1.33. Reprinted with permission from Ding et al., Matter Radiat. Extremes **1**, 135 (2016). Copyright 2016 the Science and Technology Information Center, China Academy of Engineering Physics.[29]

60/30W-5μm double array with the same array radius produced averaged power of only 3.56 ± 0.89 TW. This was in the transparent-array mode.[52–54] As a result, a double peak is observed in the radiation power. The time-resolved spectrum (Fig. 10[45]) obtained in the S300 experiments indicates that double-array plasmas were thermalized twice. This corresponds to the results

of X-ray images obtained by an ns-X-ray framing camera. In later experiments, we enlarged the array radius of the double array from 0.6 cm/0.3 cm to 1 cm/0.5 cm and reduced the wire diameter from 5 μm to 4.2 μm while keeping the linear load mass approximately the same. Images show that both the outer and inner arrays stagnated simultaneously and produced enhanced SXR radiation.
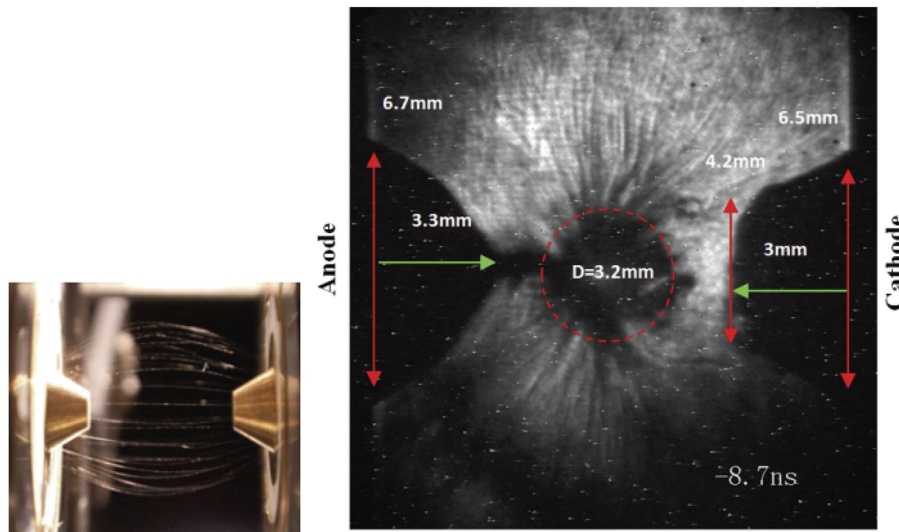

FIG. 13. Static image of preshaped load and shadowgraph of plasma density profile obtained by a 266-nm laser probe for a load with an H/D ratio of 1.1.

An averaged radiation power of 5.26 ± 0.45 TW was measured for this kind of load.

Figure 11 shows results derived from TR1DXIS images. These results could indicate how the outer-array plasma impacts on the inner one, as well as its influence on SXR power production. Figure 11(d) shows that at −4 ns relative to the current maximum, the current flow through the inner array is only 17.9% of the total load current. This indicates a rapid current switching from the outer to the inner array in a very short time [see Fig. 10(b)]. As a result, it led to rapid acceleration late in the implosion and produced the highest radiation power for a double-array load on the Angara-5 facility.

The latest experiments were performed on the Julong-1 facility using single- and double-array loads, both at a height of 15 mm. With a linear mass of ~1.3 mg/cm, the single load produced ~15-TW peak power in a duration of ~8 ns, while the double load produced ~30-TW peaked power in a much shorter pulse duration of ~4 ns. The total SXR energy was 250–350 kJ, with plasma kinetic energy, as calculated from TR1DXIS results assuming all the load mass is accelerated inward, varying from 100 to 150 kJ in different shots.
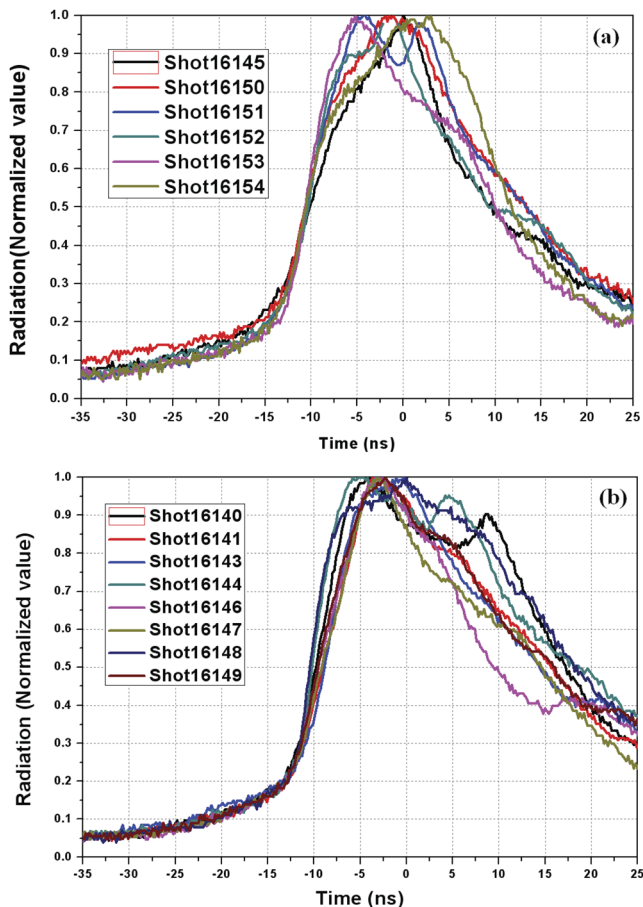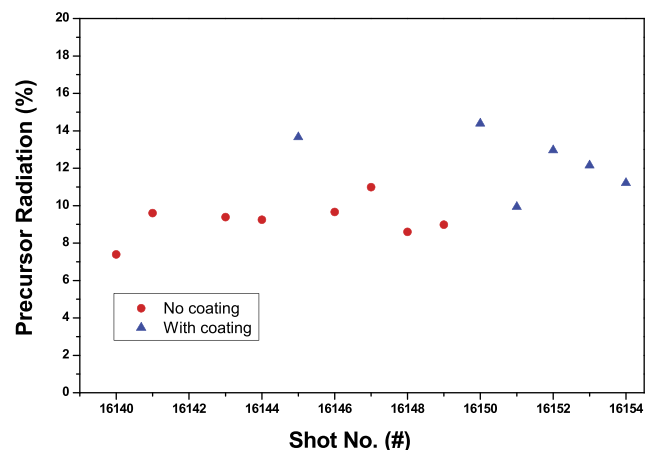
C. Quasi-spherical (QS) implosions

The energy transition from the imploding Z-pinch plasma to the cylindrical low-density foam convertor is one of the key aspects of a ZPDH, and the uniform high-temperature hohlraum radiation that is created within the hohlraum can be used to irradiate an ICF capsule. Thus, research into more effective use of the kinetic energy of a cylindrical plasma is of interest.

One potential approach is to change the cylindrical implosion into a spherical one in which the plasma concentrates at the center, instead of on the axis of symmetry.[55] Theoretical analysis gives an inward radiative flux σT^4 in the case of a spherical implosion that is four times greater than that for a cylindrical one. Numerical simulations[56] showed that in a spherical DH system, the hohlraum radiation temperature increases considerably. A double-shell QS system has even been proposed for the 26–28-MA ZR machine.

Since the magnetic field on the surface of a spherical load is naturally nonuniform, it is difficult to maintain the spherical configuration when the plasma is accelerated inward toward the center. One method is to modulate the areal mass density along the latitude θ as $m(\theta) \propto 1/\cos^2\theta$. However, this poses a great challenge for load manufacture. Previous attempts on the Angara-5-1[55] and MAGPIE generators, using spherical arrays generated by the static electric field of an additional ring electrode without any mass modulation, did not provide evidence of QS implosions with wire arrays.

We developed a new approach to obtain a spherical configuration of the imploding plasma. In this approach, mass modulation is not necessary. The initial shape of the load is nearly ellipsoidal rather than spherical. When the initially ellipsoidal plasma is accelerated to a specified radius (usually the radius of the spherical hohlraum surface) by the nonuniform magnetic field along the latitude direction, it turns into a spherical plasma shell. By changing the ratio of load height to load diameter (H/D), spherical configurations can be formed at different radii. This is called shape modification.[57]

Test experiments were performed on the Qiangguang-1 facility. A single array was made initially ellipsoidal through a static electric
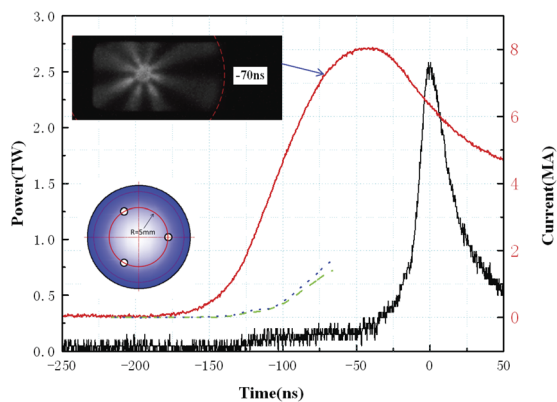

FIG. 14. SXR pulses for different shots plotted together for (a) polyimide-coated and (b) noncoated loads. Time $t = 0$ corresponds to the moment when the SXR power reaches its maximum for one of these shots. The other curves were co-aligned about half way up their rise.

FIG. 15. Ratio of early-stage radiation energy to total energy. The average over different shots gives 9.2% ± 1.0% for the uncoated load and 12.4% ± 1.6% for the polyimide-coated load, with the higher value for the latter being due to the poor coating quality.
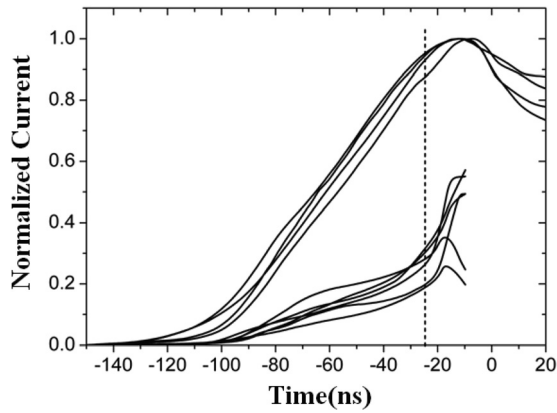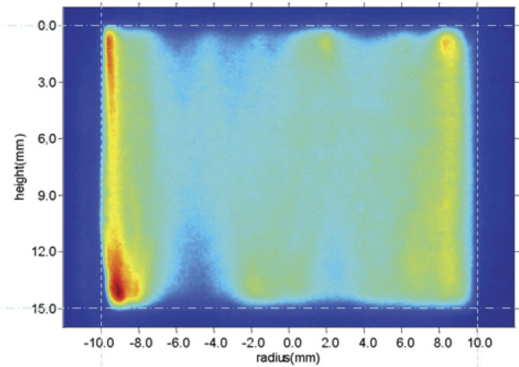
FIG. 16. Precursor current flow measured by micro magnetic probes on the Qiangguang-1 facility for four shots of the single load N42W4.2. There were two opposite magnetic probes in each shot, but two of these eight probes did not work correctly. All these probes were installed 2.7 mm from the load axis.

FIG. 18. Radiation intensity of side-on UV self-emission images taken at −136 ns.

field exerted between the metal wires and the conical electrodes. A UV framing camera, an ns-X-ray framing camera, and a 266-nm laser probe were used to observe the dynamics. Figures 12[29] and 13 show results from these experiments together with static images of the initial ellipsoidal load. The time coordinates in these two figures are relative to the SXR maximum. Three different plasma profiles can be seen as the ratio H/D is varied, and there is good consistency in terms of dynamics with 2D MHD numerical simulations. The plasma distribution near stagnation indicates a good spherical configuration as expected, despite the difficulty in achieving high quality with this kind of load. These results confirm that it is feasible to get QS implosions with appropriately preshaped wire arrays. However, the quality of these loads need to be further improved so that a spherical implosion with a more symmetric configuration can be achieved.

D. Radiation characteristics of a wire array with insulating coating

Experimental results have shown that the basic ablation processes are very similar for wire-array loads at different current levels from 1 to 26 MA.[58–63] In the ablation phase, individual wire plasmas will form a typical "wire-core" structure.[58] The ablation plasmas are
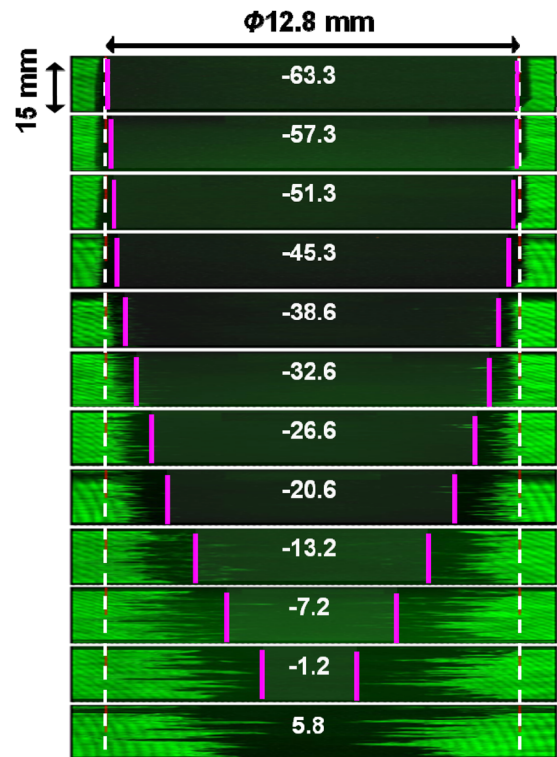

FIG. 17. Current flow inside the liner (green and blue dashed lines), total load current (red line), and SXR power (black line) are plotted together. The end-on UV self-emission image shows the appearance of precursor plasma at −70 ns for the 10-mm-radius liner. The circular dashed line in the image indicates the initial position of the liner. The radial shadow in the image was produced by spoke-like connecting electrodes.

FIG. 19. Shadowgraphs obtained by a side-on laser probe showing the evolution of the plasma density profile during liner implosion. The white dashed lines show the initial position of the liner. The pink lines indicate the predicted position of the liner plasma using a 0D code. The numbers are the times (ns) relative to the SXR maximum.
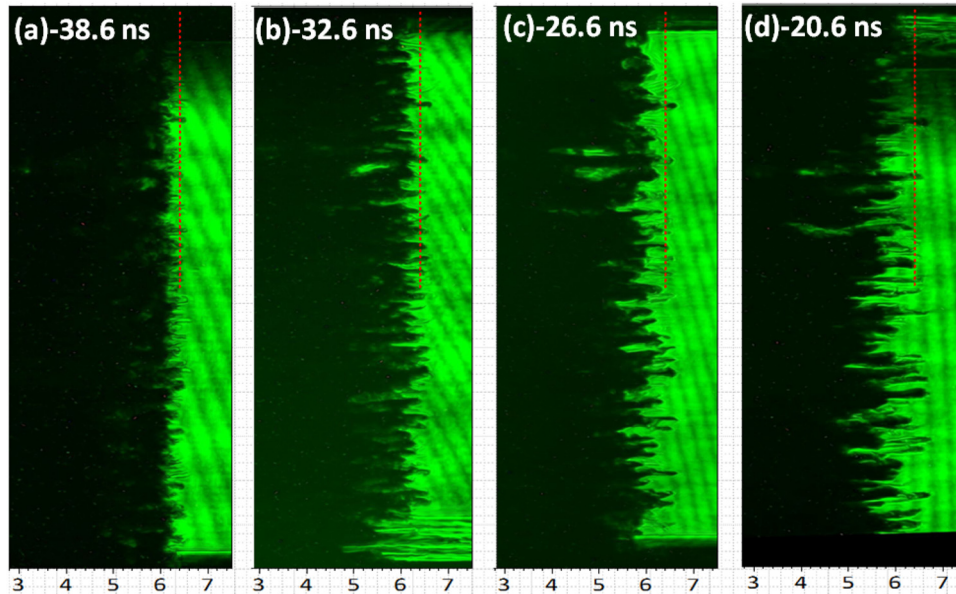
FIG. 20. Four of the images from Fig. 19 showing significant growth of RT instability while the liner plasma starts to be accelerated inward with average amplitudes of (a) 610 μm, (b) 940 μm, (c) 1150 μm, and (d) 1440 μm at the indicated times relative to the SXR maximum. The dotted lines indicate the initial position of the thin-foil liner.

accelerated toward the array axis by the global magnetic field and accumulate to form a precursor column, while the cold dense wire cores stay at their initial positions for almost 70% of the whole implosion time. This prolonged ablation dynamics determines the initial distribution of mass and current density and plays an important role in the implosion dynamics.

The dynamics of the local corona is dominated by the local magnetic field of each individual wire, in contrast to the ablation plasma that has been driven toward the array axis by the global magnetic field of the array, where the global magnetic field can dominate the local magnetic field. The physical criterion that divides the local corona plasma from the ablation plasma is the approximate equality of local and global magnetic fields in the vicinity of the wire.[64,65]

The effects of a current prepulse on the ablation process were investigated on the MAGPIE[66,67] and ZEBRA[68,69] facilities. The results show that remarkable magneto-RT (MRT) instabilities were seeded by a long prepulse and resulted in reduced radiation power. A shortened prepulse will increase the rise rate of the current flowing through each tungsten wire. Also, more energy can deposit in the wires before the wire core breaks down. As a result, SXR radiation power increased with shortened pulse duration. Further experiments with appropriate prepulses showed fully vaporized wires during the ablation phase.[14]

Sinars et al.[70] showed that when insulating coatings were added to the surfaces of individual wires, the duration of Ohmic heating in the wires was prolonged. More energy would then deposit in each individual wire before its breakdown, suppressing the effect of a prolonged core–corona ablation process. Experiments showed corona-free explosions with polyimide-coated tungsten wires driven by a current at a rise rate of ~15 kA/s.[71,72]

On the Qiangguang-1 facility, the implosion dynamics of single arrays using coated and uncoated tungsten wires, respectively, were compared. Two kinds of load were used. The first was the widely used N32W5 load (see Sec. III B, Fig. 8, and Ref. 22). The second had the same array parameters, but the wires were coated with polyimide at a thickness of ~2 μm. It must be said that the quality of the coatings was rather poor, in contrast to the fineness of the uncoated wires. There were lots of polyimide drops along each wire.

Driven by a load current of 1.23 ± 0.05 MA, the coated load produced as much SXR radiation as the uncoated one, i.e., 0.35 ± 0.024 TW
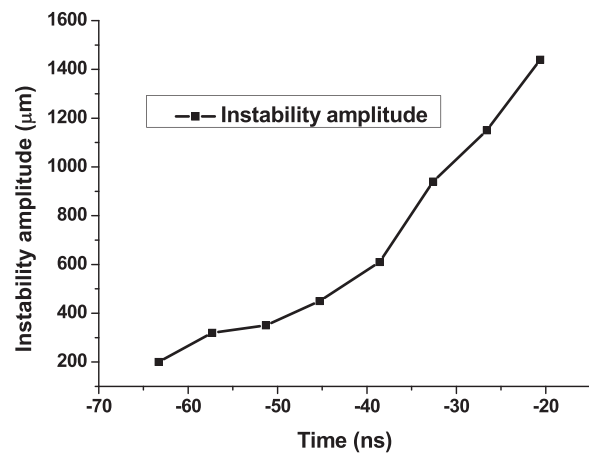

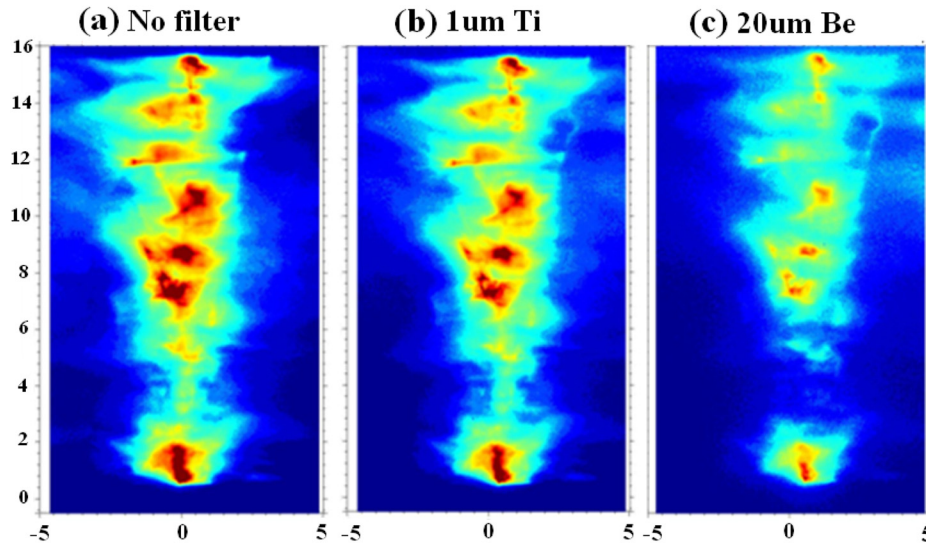**FIG. 21.** Average amplitude of RT instability at different times for the images shown in Fig. 19.

FIG. 22. Time-integrated pinhole X-ray images: (a) without filter; (b) filtered by 1-μm-thick Ti; (c) filtered by 20-μm-thick Be.

vs 0.37 ± 0.023 TW, and repeatability was excellent despite the poor coating quality. A comparison with the results shown in Fig. 7, where the initial state of a wire array load exerts a significant influence on SXR power production, confirms that a properly coated wire array load could improve the ability to produce high-power and stable SXR radiation.

The SXR pulses shown in Fig. 14 reveal the advantages of the coated load in terms of implosion dynamics. There is very good agreement at both the leading and trailing edges of the SXR pulses, despite the fairly poor quality of the coatings. The differences around the peak may be due to the nonuniform distribution of coating mass along the array axis. However, the pulses from the uncoated arrays,
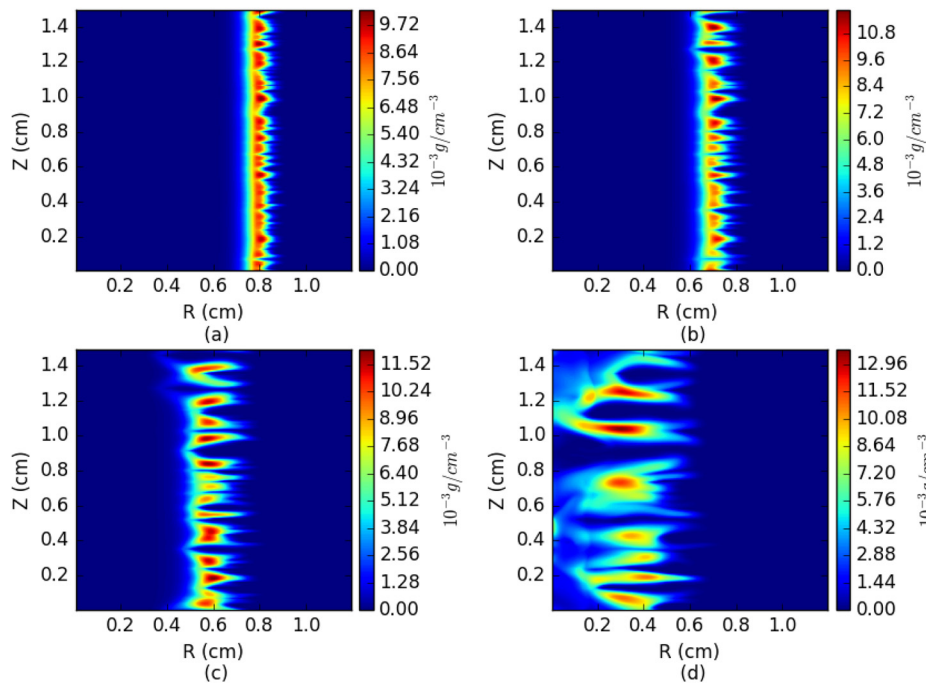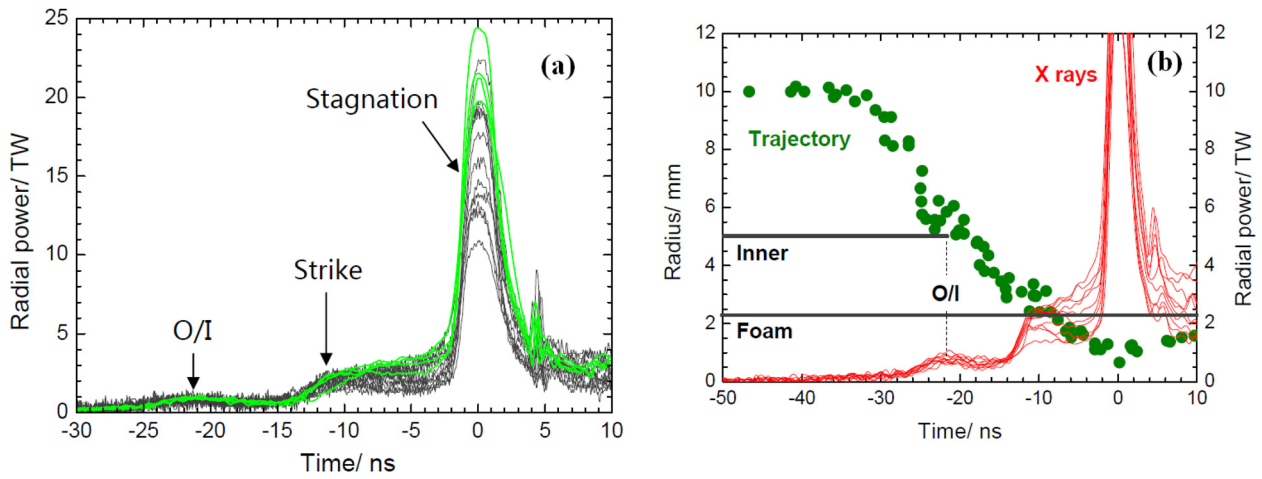

FIG. 23. Simulated growth when the measured initial seeds of RT instability are input into a 2D MHD code.

FIG. 24. (a) Radial SXR power pulses of 12 shots for the same ZPDH load. As observed by side-on cameras, "O/I" indicates the moment of interaction between outer- and inner-array plasmas, while "Strike" indicates the impact of the imploding plasma on the surface of the foam convertor. (b) Typical trajectory derived from a TR1DXIS image. SXR pulses of each shot are also plotted.
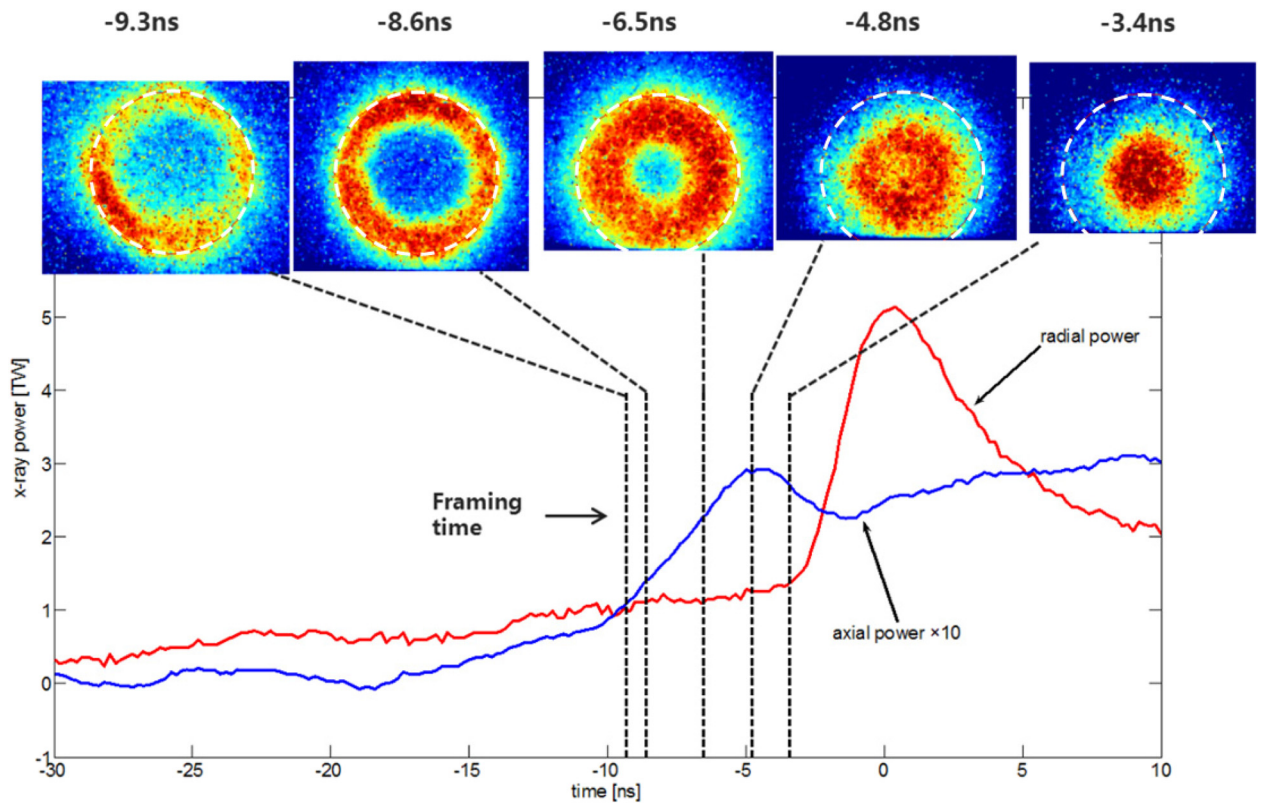
FIG. 25. A set of end-on X-ray images using an exposure of ~1 ns taken at different times (as indicated by the black dashed lines) in shot 181. Radial and axial X-ray radiation powers are plotted together. The red dashed lines in the X-ray images indicate the initial position of the 3.8-mm-diameter REH.

even with fine wire quality, deviate greatly from each other after stagnation.

It also can be seen from Fig. 14 (prior to −12 ns) that a well-manufactured load gives nearly coincident early-stage radiation, i.e., ablation dynamics, for different shots. We have plotted the ratio of early-stage radiation energy to total energy for different shots in Fig. 15. There is a noticeable increase in precursor radiation with the use of insulating coated wires, resulting from the poor coating quality.

E. Liner implosions

The precursor is formed from the corona plasma when this is driven radially inward from individual wires by the global magnetic field. A significant fraction of current will flow through the precursor plasma (see Fig. 16). A light liner implosion was therefore proposed to avoid the generation of precursor plasma, as well as with the intention of improving the density of the imploding plasma. The first attempts at light liner implosions were made on the Qiangguang-1 facility using ribbon arrays.[73] Restricted to small current and relatively overweight load mass, the results were unsatisfactory.

Further experiments were performed on the Julong-1 facility. Aluminum foils of thickness 2.0 ± 0.15 μm were used to make the thin-shell liners. These liners had the same height of 15 mm, but different radii of 6.4 or 10 mm. The roughness of the foils varied from 520 to 950 nm for different samples. The linear mass of the liners was 2.2 mg/cm. The current maximum varied from 6.4 to 6.7 MA in different shots. The corresponding SXR power maxima for these shots differed by more than 40%, although the pulse shapes were about the same.

Three micro magnetic probes positioned on a 5-mm-radius concentric circle were used to measure the current division inside the liner. A small fraction of current was measured at −120 ns prior to the SXR maximum, and increased gradually to ~20% of the total current at −70 ns (see Fig. 17), which was close to the best result obtained in wire-array experiments, as indicated by Fig. 16. At −136 ns, side-on UV self-emission images show the radiation region to be discontinuous in the radial direction (see Fig. 18). At −70 ns, an end-on UV framing camera showed that low-density plasmas were still present, focused on the axis and carrying the inner current. The reason for this may lie in the presence of the seam that occurs when a planar foil is folded and connected to form a cylindrical thin-shell liner, since luminescence was first observed to appear at this position. As confirmation, experiments on Qiangguang-1 using a liner load with four diagnostic seams (1 mm wide) produced a much greater inner current. New methods to make liners without such seams are now under consideration.

Laser shadowgraphs (see Figs. 19 and 20) show the dynamics and growth of instability during the implosion of a thin-foil liner. The bubbles of imploding plasma coincide well with the results of 0D simulation until maximum convergence. Significant growth of RT instability was observed and is plotted in Fig. 21. The average amplitude increased to 1.44 mm at −20 ns, and the maximum amplitude exceeded 3 mm at stagnation.

The shadowgraphs in Fig. 19 indicate that the stagnated plasma is distributed in a wide region with a radius of about 3 mm. However, time-integrated pinhole X-ray images (see Fig. 22) show a much smaller region of radius only half that derived from the shadowgraphs. This can be explained by 2D numerical simulation. On

inputting the measured seeds of RT instability into a 2D MHD code, it is found that the simulated plasma is distributed over a wide region owing to significant growth of RT instability (see Fig. 23). The amplitude of the RT instability exceeds the stagnated radius of the plasma. Thus, the stagnated plasma is divided into several parts along the load axis, which agrees well with the pinhole images shown in Fig. 22.

Although preliminary attempts failed to control instability growth and showed poor reproducibility, further planned experiments using liners with better coatings are worthwhile, since experiments have shown that relatively thick insulating coatings could suppress liner instabilities.[74,75] Nested and hybrid configurations, such as an outer array with an inner liner, are under serious consideration to greatly reduce the instability amplitude using the interaction between outer and inner plasmas, provided that it is possible to control the current flow in the inner array and achieve rapid current switching, which has been demonstrated in previous experiments (see Fig. 11). On the other hand, both insulating coatings and nested load configurations are beneficial in increasing the density of imploding plasmas, thus meeting the needs of a ZPDH-driven volume ignition target.

IV. DYNAMIC HOHLRAUM

In a ZPDH, the fusion capsule is strongly coupled to the overall Z-pinch implosion. The arrival of the convertor shock on axis may fatally crush the capsule and destroy the symmetry of compression. It is therefore necessary to complete the implosion of the capsule before arrival of the shock. In this section, we present the latest experimental results on the properties of hohlraum radiation and the propagation of shock waves on the Julong-1 facility.

In these experiments, the radial radiation power was monitored by a side-on SXRPM. Axial radiation power escaping from the upper radiation exit hole was measured at 8° with respect to the Z-pinch axis using an SXRPM and XRD. Shock propagation was observed using an end-on X-ray framing camera with or without filters. An optical
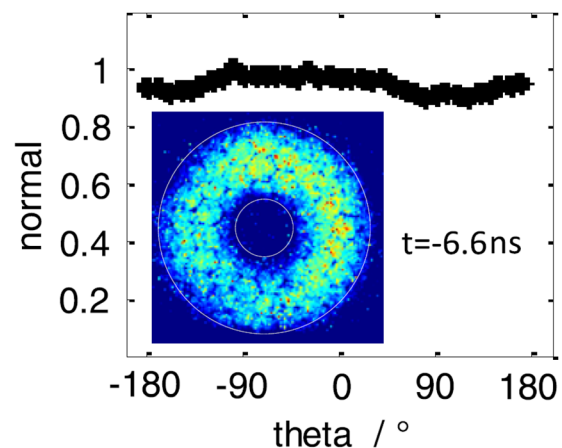
FIG. 26. Azimuthal distribution of the averaged intensities of the shock, in the region between two concentric white dashed circles in the image, at −6.5 ns in shot 181. Reprinted with permission from Meng et al., Phys. Plasmas **24**, 014505 (2017). Copyright 2017 AIP Publishing LLC.[76]

streak camera and TR1DXIS were used for side-on trajectory measurements.

Different ensembles of wire arrays with low-density foams were investigated. The nested array, of height 15 mm and outer/inner
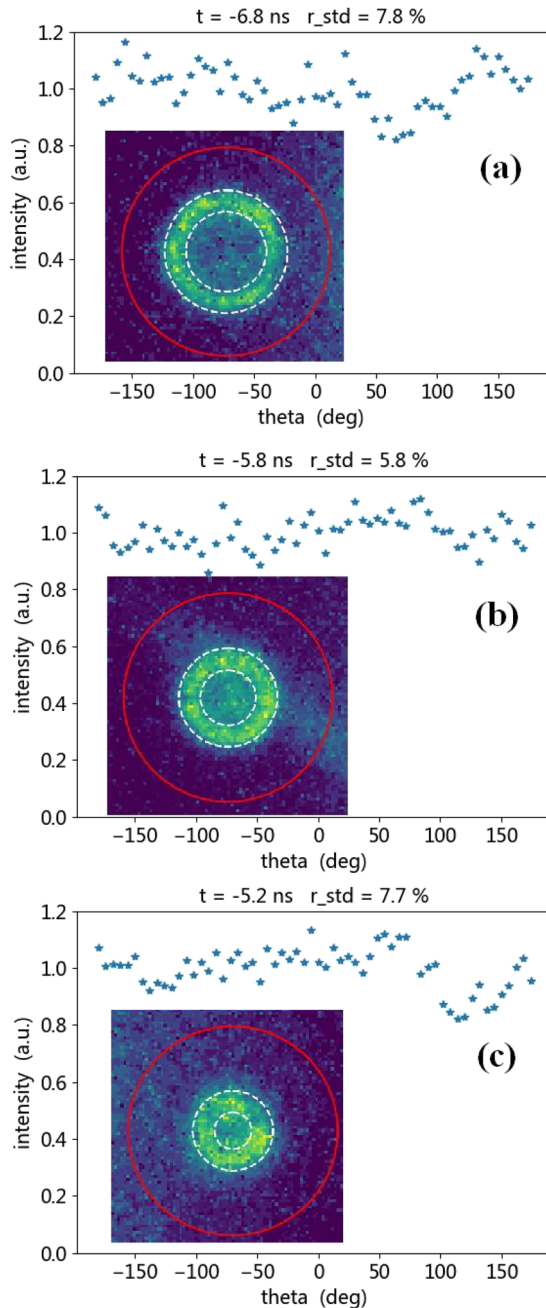

FIG. 27. Filtered X-ray images of the shock obtained in shot 335 with a 10-μm-thick beryllium filter. The red circles indicate the initial position of the REH. The azimuthal asymmetry in the shock region between the two concentric white dashed circles is ~7.8% at −6.8 ns, ~5.8% at −5.8 ns, and ~7.7% at −5.2 ns.

radius 10 mm/5 mm, with 168/84 6-μm-diameter wires in the outer/inner array, driving a foam convertor of radius 2.3 mm and density 10 mg/cm^3, showed good repeatability before the majority of the imploding plasma interacted with the foam as in Fig. 24(a). The interaction between the outer and inner array plasmas occurs at about −22 ns relative to the SXR maximum. This produces weak radiation. When the plasma impacts on the foam convertor at about −10 ns, a radiation platform is observed in every shot. The trajectory in Fig. 24(b) shows excellent coincidence with the SXR results for this dynamical process.

Figure 25 shows a set of time-resolved end-on X-ray images of the shock in one shot (shot 181). The corresponding radial radiation power from the imploding plasma and the axial radiation power emitted from the radiation exit hole (REH) are plotted together. Meng *et al.*[76] give the velocity of the inward-propagating shock in this shot as 31.9 ± 5.6 cm/μs, as inferred from a linear fit of the trajectory. The radial thickness of the annual shell is estimated to be ~1.0 mm.

The azimuthal symmetry of the shock in shot 181 can be seen in Fig. 26.[76] The intensity of the shock as a function of azimuthal angle is measured from the images captured by the end-on camera. The shock, indicated by two concentric white dashed circles in the image in Fig. 26, is divided into 36 equal sectors. The relative standard deviation of the azimuthal distribution is then estimated to be ~3% at this time.

Figure 27 shows typical filtered end-on X-ray images from a 10-μm-thick beryllium filter in the X-ray framing camera. The azimuthal asymmetry derived from these images is in the range 6%–8%, which is somewhat poorer than the unfiltered results in shot 181.
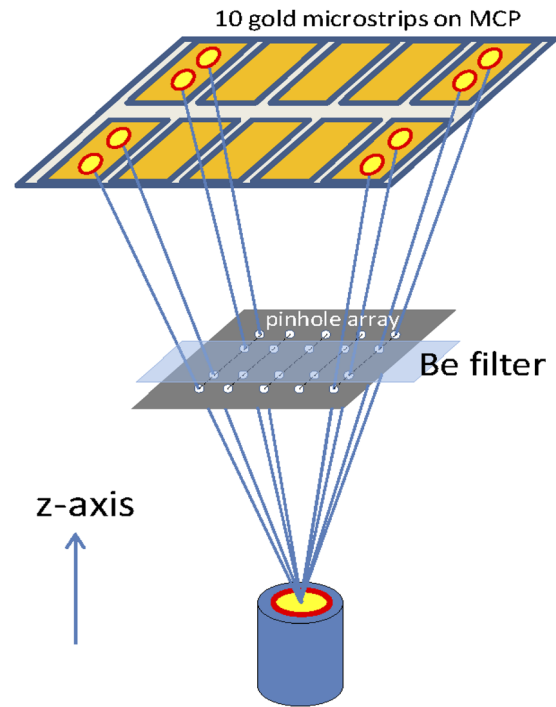
FIG. 28. Schematic of the end-on X-ray framing camera used to observe shock propagation simultaneously with and without filters.
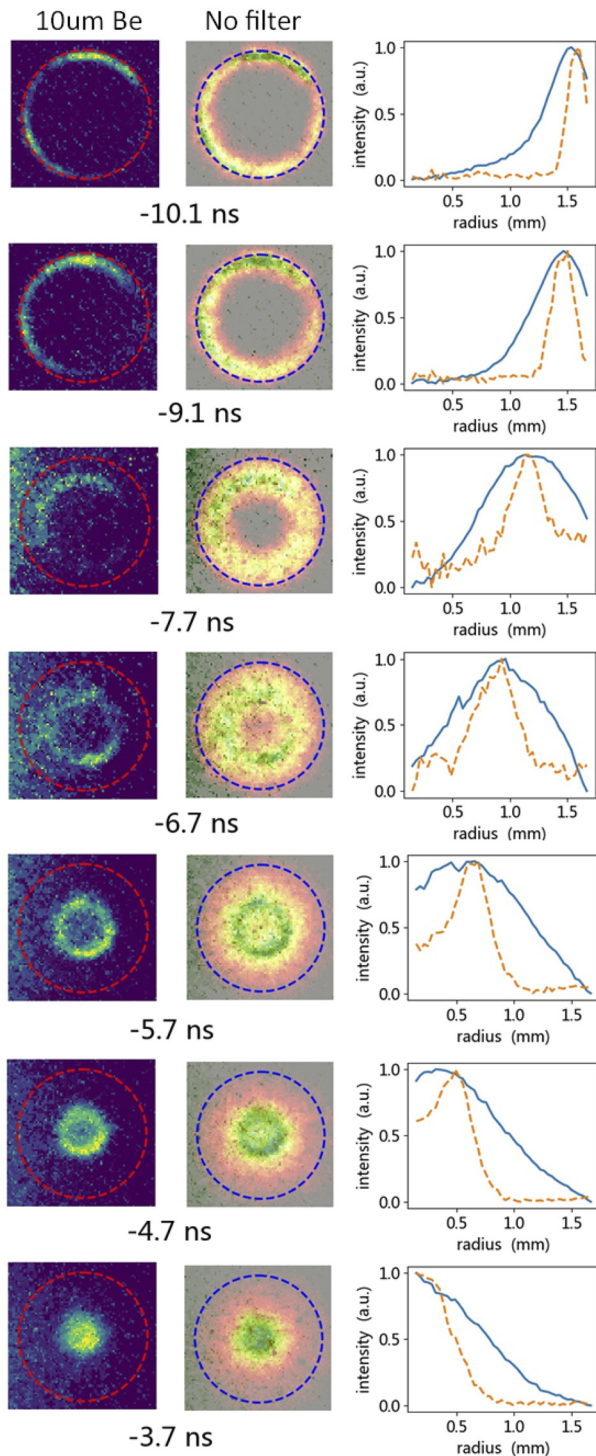
FIG. 29. End-on X-ray images observed in shot 336 from the REH with and without filters. The dashed circles indicate the initial position and profile of the REH. The curves in the right column are the results of the average radiation intensities with and without filters as functions of radius. $r = 0$ represents the center of the dashed circles in these images.

In later experiments, both filtered and unfiltered X-ray images were taken by the X-ray framing camera using a new pinhole array as shown in Fig. 28. Direct comparison and analysis of the differences between the filtered and unfiltered results are thus available. Figure 29 shows a typical result obtained in shot 336. It indicates widely spreading plasmas along the radius. When the low-density plasma in the imploding plasma front impacts first on the foam convertor, a weak shock wave is generated and propagates inward. After 2–3 ns, the main shock, which is much smaller in radial width, generated by relatively high-density plasma, catches the previous one. Radiation generated by the intense shock increases in temperature and is rapidly transported inward. This also indicates that the main shock had a radial width of less than 0.5 mm. This is good news for a capsule in a ZPDH in that the transformation from kinetic energy of the imploding plasma to radiation energy in the hohlraum could be finished within 2 ns in a specially optimized liner implosion, since the shock velocity is ~23 cm/μs. It is of great benefit for the symmetry of irradiation on the ablator surface of a capsule prior to arrival of the shock.

The variations of shock position and hohlraum radiation temperature are shown in Fig. 30. The main shock has an approximately constant velocity of 23 ± 1.4 cm/μs. Before the shock converges on the axis, the radiation temperature rises to ~110 eV.

It is assumed that the radiation in the foam is an ideal blackbody source, so its spectrum out of the REH is Planckian. By azimuthally averaging the radiation temperature as a function of radius, time-resolved radial distributions of temperature at different times can then be obtained (see Fig. 31). When the shock has just entered the REH at −8.4 ns, the radiation temperature in the shocked region is ~70 eV. As the shock wave converges, the radiation temperature increases. At the moment at which the axial radiation reaches its maximum, the peak radiation temperature is about 100 eV. When the shock reaches the axis, the radiation temperature peaks at ~110 eV in shot 198. Furthermore, Fig. 31 also indicates that plasma–foam interaction could be finished within ~3 ns (−8.4 to −5.4 ns), which is one of the key reasons why indirect drive is needed, especially for a spherical capsule centered in a cylindrical hohlraum.
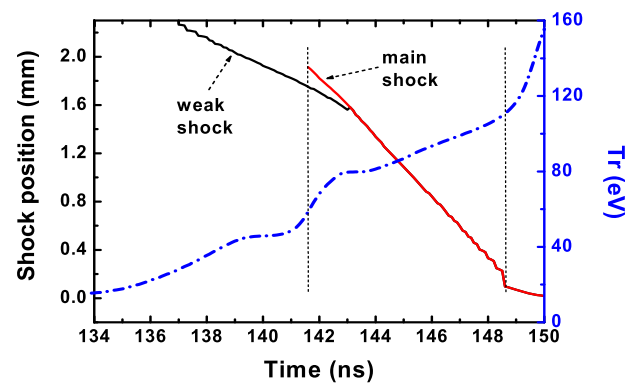
FIG. 30. Variations of shock position, derived from the TR1DXIS image, and radiation temperature inside the hohlraum in shot 335.
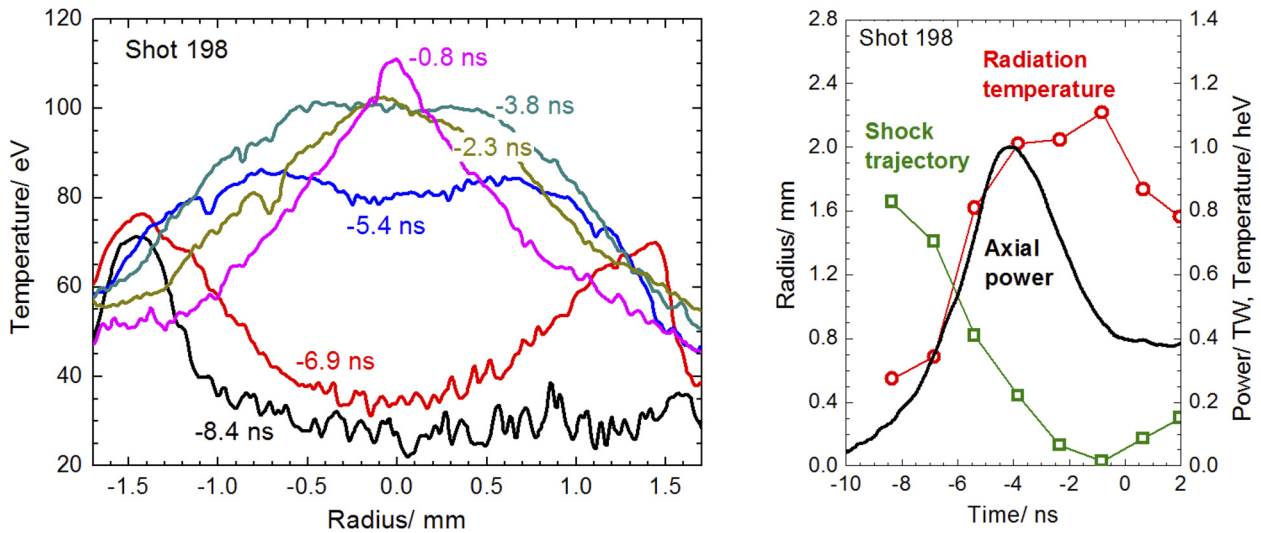
FIG. 31. (a) Radial distributions of radiation power at different times in shot 198. (b) Shock trajectory obtained from framing X-ray images together with variations of axial radiation power and radiation temperature.

V. CONCLUSION

We have presented an overview of experimental investigations of wire-array Z-pinches and dynamic hohlraums performed at the Institute of Nuclear Physics and Chemistry, China Academy of Engineering and Physics. Technical requirements for Z-pinches and dynamic hohlraums for a newly developed target concept, together with its basic performance, have been described. Progress in optimization of SXR radiation over a wide current range, as well as density profile modulation, have been described. The implosion dynamics of nested wire arrays, quasi-spherical wire arrays, and thin-foil liners have been studied as alternatives for driving volume ignition targets. Recently, more attention has been paid to the study of ZPDHs. In a first step, fundamental aspects of performance, such as implosion dynamics, plasma–foam impact, shock propagation, and hohlraum radiation production have been investigated and results have been presented.

In the near future, our attention will turn to the plasma density profile with a high impact density using nested and hybrid liner loads, shock and hohlraum radiation modulation using a combined foam convertor, integrated experimental studies of plasma–foam energy coupling efficiency, and compression symmetry of a DH-irradiated simulated target. The integrity of the relatively thin shell in a target when it undergoes a shock needs to be considered carefully, together with the growth of interface instabilities.

ACKNOWLEDGMENTS

REFERENCES

[1] R. B. Spielman et al., "Tungsten wire-array Z-pinch experiments at 200TW and 2 MJ," Phys. Plasmas **5**, 2105–2111 (1998).

[2] W. A. Stygar et al., "Theoretical z-pinch scaling relations for thermo-nuclear-fusion experiments," Phys. Rev. E **72**, 026404 (2005).

[3] T. J. Nash, M. S. Derzon, G. A. Chandler et al., "High temperature dynamic hohlraums on the pulsed power driver Z," Phys. Plasmas **6**, 2023–2029 (1999).

[4] S. A. Slutz, M. R. Douglas, J. S. Lash et al., "Scaling and optimization of the radiation temperature in dynamic hohlraums," Phys. Plasmas **8**, 1673 (2001).

[5] J. Bailey, G. Chandler, S. Slutz et al., "X-ray imaging measurements of capsule implosions driven by a Z-pinch dynamic hohlraum," Phys. Rev. Lett. **89**, 095004 (2002).

[6] S. A. Slutz, J. E. Bailey, G. A. Chandler et al., "Dynamic hohlraum driven inertial fusion capsules," Phys. Plasmas **10**, 1875–1882 (2003).

[7] J. H. Hammer, M. Tabak, S. C. Wilks et al., "High yield inertial confinement fusion target design for a z-pinch-driven hohlraum," Phys. Plasmas **6**, 2129 (1999).

[8] G. R. Bennett, M. E. Cuneo, R. A. Vesey et al., "Symmetric inertial-confinement-fusion-capsule implosions in a double-z-pinch-driven hohlraum," Phys. Rev. Lett. **89**, 245002 (2002).

[9] G. A. Rochau, J. E. Bailey, G. A. Chandler, G. Cooper, G. S. Dunham et al., "High performance capsule implosions driven by the z-pinch dynamic hohlraum," Plasma Phys. Controlled Fusion **49**, B591 (2007).

[10] S. A. Slutz, M. C. Herrmann, R. A. Vesey et al., "Pulsed-power-driven cylindrical liner implosions of laser preheated fuel magnetized with an axial field," Phys. Plasmas **17**, 056303 (2010).

[11] M. R. Gomez, S. A. Slutz, A. B. Sefkow et al., "Experimental demonstration of fusion-relevant conditions in magnetized liner inertial fusion," Phys. Rev. Lett. **113**, 155003 (2014).

[12] J. A. Cobble and D. B. Sinars, A 1-D Study of the Ignition Space for Magnetic Indirect (X-ray) Drive Targets, A white paper for NNSA, Report No. LA-UR-16-24652, July 6, 2016.

[13] L. B. Yang, H. D. Liao, C. W. Sun, K. Ouyang, J. Li et al., "RT instability in cylindrical implosion of jelly ring," Chin. Phys. **13**, 1747 (2004).

[14] H. T. Shi, X. B. Zou, and X. X. Wang, "Fully vaporized electrical explosion of bare tungsten wire in vacuum," Appl. Phys. Lett. **109**, 134105 (2016).

[15]X. L. Zhu, S. Zhao, X. B. Zou, H. T. Shi, H. Y. Luo, and X. X. Wang, "The development of coated and non-coated wire explosions observed by X-ray back-lighting," Phys. Plasmas **22**, 112707 (2015).

[16]X. L. Zhu, X. B. Zou, S. Zhao, H. T. Shi, R. Zhang, H. Y. Luo, and X. X. Wang, "Measuring the evolution of mass density distribution of wire explosion," IEEE Trans. Plasma Sci. **42**, 2522 (2014).

[17]K. Wang, Z. Q. Shi, Y. J. Shi, J. Wu, and S. L. Jia, "Study on the energy deposition in fast electrical explosion of single aluminum wire in vacuum," in XXVI International Symposium on Discharges and Electrical Insulation in Vacuum, Mumbai, India, 2014.

[18]M. Li, L. Sheng, L. P. Wang et al., "The effects of insulating coatings and current prepulse on tungsten planar wire array Z-pinches," Phys. Plasmas **22**, 122710 (2015).

[19]L. Sheng, Y. Li, Y. Yuan, B. D. Peng, M. Li et al., "Experimental study of insulated aluminum planar wire array Z pinches," Acta Phys. Sin. **63**, 055201 (2014).

[20]L. Wang, J. Wu, N. Guo, J. Han, M. Li et al., "Investigation of the resistance and inductance of planar wire array at Qiangguang accelerator," Plasma Sci. Technol. **14**, 842–846 (2012).

[21]R. K. Xu, Z. H. Li, J. L. Yang, X. W. Zhou, S. L. Jiang et al., "New results of Sino-Russian joint Z-pinch experiments," Acta Phys. Sin. **60**, 045208 (2011).

[22]Z. Wang, Z. H. Li, R. K. Xu, J. L. Yang, N. Ding et al., "X-ray radiation power optimization in 1MA to 4MA wire-array implosions," Acta Phys. Sin. **60**, 025209 (2011).

[23]J. Deng, W. Xie, S. Feng, M. Wang, H. Li et al., "Initial performance of the primary test stand," IEEE Trans. Plasma Sci. **41**, 2580–2583 (2013).

[24]W. Zou, F. Guo, L. Chen, S. Song, M. Wang et al., "Full circuit calculation for electromagnetic pulse transmission in a high current facility," Phys. Rev. Spec. Top.–Accel. Beams **17**, 110401 (2014).

[25]X. J. Peng, "Design of a Z-pinch driven inertial confinement fusion target," internal report (unpublished).

[26]Y. K. Zhao, B. Y. Ouyang, W. Wen, and M. Wang, "Critical value of volume ignition and condition of nonequilibrium burning of DT in inertial confinement fusion," Acta Phys. Sin. **64**, 045205 (2015).

[27]X. J. Peng, "Z-pinch fusion-fission hybrid reactor—The energy technology road with great competitive power," J. Southwest Univ. Sci. Tech. **25**, 1 (2010).

[28]X. J. Peng and Z. Wang, "Conceptual research on Z-pinch driven fusion-fission hybrid reactor," High Power Laser Part. Beams **26**, 90201 (2014).

[29]N. Ding, Y. Zhang, D. L. Xiao, J. M. Wu, Z. H. Dai et al., "Theoretical and numerical research of wire array Z-pinch and dynamic hohlraum at IAPCM," Matter Radiat. Extremes **1**, 135 (2016).

[30]R. Ramisa and J. Meyer-ter-Vehn, "MULTI-IFE—A one-dimensional computer code for Inertial Fusion Energy (IFE) target simulations," Comput. Phys. Commun. **203**, 226 (2016).

[31]Y. Y. Chu, Z. Wang, J. M. Qi, F. Y. Wu, Z. H. Li et al., "Numerical simulation on a new cylindrical target for Z-pinch driven inertial confinement fusion," Nucl. Fusion **57**, 066019 (2017).

[32]S. L. Jiang, J. M. Ning, R. K. Xu, Z. H. Li, C. Guo et al., "Scintillant detection system for Z-pinch X-ray radiation power," At. Energy Sci. Tech. **40**, 96 (2006).

[33]Q. Y. Hu, J. M. Ning, F. Ye, S. J. Meng, R. K. Xu et al., "A free-standing thin foil bolometer for measuring soft x-ray fluence," Rev. Sci. Instrum. **87**, 103302 (2016).

[34]G. X. Xia, Z. P. Xu, R. K. Xu, J. C. Chen, and F. Q. Zhang, "Application of framing camera in wire array Z-pinch experiments," Nucl. Electron Detect. Technol. **27**, 966 (2007).

[35]Z. Wang, J. L. Yang, R. K. Xu, L. B. Li, Z. P. Xu et al., "Framing shadowgraphy of 266nm laser probing for the diagnosis of Z-pinch plasmas," Acta Phys. Sin. **55**, 5942 (2006).

[36]Z. Wang, J. L. Yang, N. Ding, I. N. Frolov, R. K. Xu et al., "UV laser probing of imploding wire-array plasmas on the Angara-5-1 facility," IEEE Trans. Plasma Sci. **36**, 174 (2008).

[37]R. K. Xu, Z. H. Li, C. Guo et al., "One-dimensional temporal-spatial X-ray imaging system," Acta Phys. Sin. **52**, 1203–1206 (2003).

[38]D. H. Kalantar and D. A. Hammer, "The x-pinch as a point source of x-rays for backlighting," Rev. Sci. Instrum. **66**, 779 (1995).

[39]X. L. Zhu, X. B. Zou, S. Zhao, R. Zhang, H. T. Shi et al., "Mass density evolution of wire explosion observed using X-ray backlight," IEEE Trans. Plasma Sci. **42**, 3221 (2014).

[40]R. Zhang, H. Y. Luo, X. B. Zou, H. T. Shi, X. L. Zhu et al., "Energy spectrum measurement of X-ray radiation from a compact x-pinch device," IEEE Trans. Plasma Sci. **42**(10), 3143–3147 (2014).

[41]J. Wu, L. P. Wang, M. Li, G. Wu, M. T. Qiu et al., "Experimental investigations of tungsten X-pinches using the QiangGuang-1 facility," Acta Phys. Sin. **63**, 035205 (2014).

[42]G. R. Bennett, O. L. Landen, R. F. Adams et al., "X-ray imaging techniques on Z using the Z-Beamlet laser," Rev. Sci. Instrum. **72**, 657 (2001).

[43]E. Esarey, "Nonlinear Thomson scattering of intense laser pulses from beams and plasmas," Phys. Rev. E **48**, 3003 (1993).

[44]F. Ye, F. B. Xue, C. Guo, Z. H. Li, and J. L. Yang, "Utilization of convex crystal spectrograph to obtain monochromatic X-ray images of Z-pinch plasmas," Acta Phys. Sin. **57**, 1792 (2008).

[45]F. Ye, Y. Qin, S. Q. Jiang, F. B. Xue, and Z. H. Li, "A time-resolved spectroscopic diagnostic based on fast scintillator and optical fiber array for z-pinch plasmas," Rev. Sci. Instrum. **80**, 106105 (2009).

[46]F. B. Xue, J. L. Yang, and R. K. Xu, "Application of micro magnetic probe to diagnosis of load current in Z-pinch experiments," High Power Laser Part. Beams **22**, 2055 (2010).

[47]N. Ding, J. Wu, Z. H. Yang, S. W. Fu, C. Ning et al., "Simulation of Z-pinch implosion using MARED code," High Power Laser Part. Beams **20**, 212 (2008).

[48]Z. Wang, R. K. Xu, J. L. Yang, X. S. Hua, and L. B. Li, "Experimental study on imploding characteristics of wire-array Z pinches on QiangGuang-1 facility," Chin. Phys. **16**, 772 (2007).

[49]F. Q. Zhang, Z. H. Li, Z. P. Xu et al., "X-ray observations of tungsten wire array Z-pinch implosions on QiangGuang-1 facility," Chin. Phys. **15**, 2058 (2006).

[50]H. M. Cai, W. D. Wu, L. Zhang, T. Li, and X. W. Zhou, "Z-pinch wire-array micro assembly station," High Power Laser Part. Beams **09**, 1351 (2009).

[51]H. M. Cai, W. D. Wu, L. Zhang, Z. X. Huang, and X. W. Zhou, "Visual inspection technology of Z-pinch wire-array assembly parameters," High Power Laser Part. Beams **22**, 68 (2010).

[52]J. P. Chittenden, S. V. Lebedev, S. N. Bland, A. Ciardi, and M. G. Haines, "The different dynamical modes of nested wire array Z-pinches," Phys. Plasmas **8**, 675–678 (2001).

[53]N. Ding, Y. Zhang, Q. Liu, D. L. Xiao, X. J. Shu, and C. Ning, "Effects of various inductances on the dynamic models of the Z-pinch implosion of nested wire arrays," Acta Phys. Sin. **58**, 1083 (2009).

[54]M. E. Cuneo, D. B. Sinars, D. E. Bliss, E. M. Waisman, J. L. Porter et al., "Direct experimental evidence for current-transfer mode operation of nested tungsten wire arrays at 16–19 MA," Phys. Rev. Lett. **94**, 225003 (2005).

[55]V. Smirnov, S. Zakharov, and E. Grabovskii, "Increase in radiation intensity in a quasi-spherical double liner/dynamic hohlraum system," JETP Lett. **81**, 442–447 (2005).

[56]T. Nash, P. VanDevender, D. McDaniel, and L. Abbot, "Quasi-spherical direct drive fusion," Sandia National Laboratory Report No. SAND 2007–0235.

[57]Y. Zhang, N. Ding, Z. H. Li, S. Sun, C. Xue et al., "Dynamics of quasi-spherical Z-pinch implosions with mass redistribution and displacement modification," Phys. Plasmas **19**, 122704 (2012).

[58]J. P. Chittenden, S. V. Lebedev, A. R. Bell, R. Aliaga-Rossel, S. N. Bland et al., "Plasma formation and implosion structure in wire array Z pinches," Phys. Rev. Lett. **83**, 100 (1999).

[59]M. E. Cuneo, E. M. Waisman, S. V. Lebedev, J. P. Chittenden, W. A. Stygar et al., "Characteristics and scaling of tungsten-wire-array Z-pinch implosion dynamics at 20 MA," Phys. Rev. E **71**, 046406 (2005).

[60]S. V. Lebedev, F. N. Beg, S. N. Bland, J. P. Chittenden, A. E. Dangor et al., "Effect of discrete wires on the implosion dynamics of wire array Z pinches," Phys. Plasmas **8**, 3734 (2001).

[61]V. V. Alexandrov, A. V. Branitskii, G. S. Volkov, E. V. Grabovskii, M. V. Zurin et al., "Dynamics of heterogeneous liners with prolonged plasma creation," Plasma Phys. Rep. **27**, 89–109 (2001).

[62]P. V. Sasorov, B. V. Oliver, E. P. Yu, and T. A. Mehlhorn, "One-dimensional ablation in multiwire arrays," Phys. Plasmas **15**, 022702 (2008).

[63]E. P. Yu, B. V. Oliver, D. B. Sinars, T. A. M. M. E. Cuneo *et al.*, "Steady-state radiation ablation in the wire-array Z-pinch," Phys. Plasmas **14**, 022705 (2007).

[64]T. A. Shelkovenko, S. A. Pikuz, J. D. Douglass *et al.*, "Wire core and coronal plasma expansion in wire-array Z pinches with small numbers of wires," Phys. Plasmas **14**, 102702 (2007).

[65]E. P. Yu, B. V. Oliver, and D. B. Sinars, "Wire core and coronal plasma expansion in wire-array Z pinches with small numbers of wires," Phys. Plasmas **14**, 022705 (2007).

[66]F. N. Beg, S. V. Lebedev, S. N. Bland *et al.*, "The effect of current prepulse on wire array Z-pinch implosions," Phys. Plasmas **9**, 375 (2002).

[67]S. V. Lebedev, D. J. Ampleford, S. N. Bland *et al.*, "Physics of wire array Z-pinch implosions: Experiments at imperial college," Plasma Phys. Controlled Fusion **47**, A91 (2005).

[68]G. S. Sarkisov, S. E. Rosenthal, K. W. Struve *et al.*, "Effect of current prepulse on wire array initiation on the 1-MA ZEBRA accelerator," Phys. Plasmas **14**, 052704 (2007).

[69]G. S. Sarkisov, S. E. Rosenthal, K. W. Struve *et al.*, "Initiation of aluminum wire array on the 1-MA ZEBRA accelerator and its effect on ablation dynamics and x-ray yield," Phys. Plasmas **14**, 112701 (2007).

[70]D. B. Sinars, T. A. Shelkovenko, S. A. Pikuz *et al.*, "The effect of insulating coatings on exploding wire plasma formation," Phys. Plasmas **7**, 429 (2000).

[71]G. S. Sarkisov, S. E. Rosenthal, and K. W. Struve, "Corona-free electrical explosion of polyimide-coated tungsten wire in vacuum," Phys. Rev. Lett. **94**, 035004 (2005).

[72]G. S. Sarkisov, S. E. Rosenthal, and K. W. Struve, "Transformation of a tungsten wire to the plasma state by nanosecond electrical explosion in vacuum," Phys. Rev. E **77**, 056406 (2008).

[73]Z. H. Li, R. K. Xu, Y. Y. Chu *et al.*, "Experimental investigation of the ribbon-array ablation process," Phys. Plasmas **20**, 032702 (2013).

[74]K. J. Peterson, D. B. Sinars, E. P. Yu *et al.*, "Electrothermal instability growth in magnetically driven pulsed power liners," Phys. Plasmas **19**, 092701 (2012).

[75]K. J. Peterson, T. J. Awe, E. P. Yu *et al.*, "Electrothermal instability mitigation by using thick dielectric coatings on magnetically imploded conductors," Phys. Rev. Lett. **112**, 135002 (2014).

[76]S. J. Meng, Q. Y. Hu, J. M. Ning, F. Ye, Z. C. Huang *et al.*, "Measurement of axial radiation properties in Z-pinch dynamic hohlraum at Julong-1," Phys. Plasmas **24**, 014505 (2017).